

Probing the Galactic Potential with Next-Generation Observations of Disk Stars

T. Sumi¹, K.V. Johnston², S. Tremaine³, D.N. Spergel⁴ & S. R. Majewski⁵

ABSTRACT

Our current knowledge of the rotation curve of the Milky Way is remarkably poor compared to other galaxies, limited by the combined effects of extinction and the lack of large samples of stars with good distance estimates and proper motions. Near-future surveys promise a dramatic improvement in the number and precision of astrometric, photometric, and spectroscopic measurements of stars in the Milky Way’s disk. We examine the impact of such surveys on our understanding of the Galaxy by “observing” particle realizations of nonaxisymmetric disk distributions orbiting in an axisymmetric halo with appropriate errors and then attempting to recover the underlying potential using a Markov Chain Monte Carlo (MCMC) approach. We demonstrate that the azimuthally averaged gravitational force field in the Galactic plane—and hence, to a lesser extent, the Galactic mass distribution—can be tightly constrained over a large range of radii using a variety of types of surveys so long as the error distribution of the measurements of the parallax, proper motion, and radial velocity are well understood and the disk is surveyed globally. One advantage of our method is that the target stars can be selected nonrandomly in real or apparent-magnitude space to ensure just such a global sample without biasing the results. Assuming that we can always measure the line-of-sight velocity of a star with at least 1 km s^{-1} precision, we demonstrate that the force field can be determined to better than

¹Solar Terrestrial Environment Laboratory, Nagoya University, Nagoya, 464-8601, Japan
e-mail: sumi@stelab.nagoya-u.ac.jp

²Department of Astronomy, Columbia University, New York, NY 10027, USA
e-mail: kvj@astro.columbia.edu

³Institute for Advanced Study, Princeton, NJ 08540, USA,
e-mail: tremaine@ias.edu

⁴Princeton University Observatory, Princeton, NJ 08544-1001, USA,
e-mail: dns@astro.princeton.edu

⁵Department of Astronomy, University of Virginia, Charlottesville, VA 22904-4325, USA
e-mail: srm4n@virginia.edu

$\sim 1\%$ for Galactocentric radii in the range $R = 4 - 20$ kpc using either: (1) small samples (a few hundred stars) with very accurate trigonometric parallaxes and good proper-motion measurements (uncertainties $\delta_{p,\text{tri}} \lesssim 10 \mu\text{as}$ and $\delta_\mu \lesssim 100 \mu\text{as yr}^{-1}$ respectively); (2) modest samples (~ 1000 stars) with good indirect parallax estimates (e.g., uncertainty in photometric parallax $\delta_{p,\text{phot}} \sim 10\%-20\%$) and good proper-motion measurements ($\delta_\mu \sim 100 \mu\text{as yr}^{-1}$); or (3) large samples ($\sim 10^4$ stars) with good indirect parallax estimates and lower accuracy proper-motion measurements ($\delta_\mu \sim 1 \text{ mas yr}^{-1}$). We conclude that near-future surveys, like SIM Lite, Gaia, and VERA, will provide the first precise mapping of the gravitational force field in the region of the Galactic disk.

Subject headings: dark matter – Galaxy:disk – Galaxy:fundamental parameters
 – Galaxy: kinematics and dynamics – methods: data analysis – surveys

1. Introduction

Observations of the motions of stars and gas in galaxies tell us that they contain many times more mass in encompassing dark matter halos than in their stellar components (e.g., Kent 1987). However, exactly how this dark matter is actually distributed in galaxies is still of some debate. For example, while simulations of cold dark matter halos forming in an expanding universe seem to generally converge on a density distribution that can be represented by a universal formula (Navarro et al. 1996, 1997), the shape and radial profile of the inner parts of dark matter halos are still uncertain (see discussion in Navarro et al. 2004; Hayashi et al. 2004).

Of course, baryons are expected to complicate the elegant simplicity of the picture of dark matter halos painted by pure N -body simulations. Gas radiates away energy to sink toward the centers of the dark matter halos where it can contribute significantly to the gravitational potential. This process can cause the background dark matter halo to contract further in response (as reviewed in Gnedin et al. 2004) and evolve from triaxial to more spherical in shape (Dubinski 1994; Kazantzidis et al. 2004; Bailin et al. 2005; Abadi et al. 2009). On the other hand, stellar bars at the centers of galaxies can transfer angular momenta to their host halos, flattening their central density cusps (Sellwood 2006). The decay of satellite galaxies and substructure can also flatten the central density cusps.

Ultimately, we want to be able to distinguish between dark and luminous contributions to the distribution of matter throughout galaxies. Stellar disks provide some of the cleanest probes of matter distributions, with stars moving on near circular orbits. Nevertheless, there

remains the tricky problem of decomposing a disk galaxy potential into disk, bulge and halo contributions in order to isolate the form of the dark matter distribution. One approach to this dilemma has been to look at low-surface-brightness galaxies, which are expected to be dominated by dark matter, yet even in these cases the results have been controversial and ambiguous (see de Blok 2005; Hayashi et al. 2004, for two opposing views)

It is striking that our own Milky Way galaxy has as yet contributed little to these debates. After all, this is the one galaxy we can expect to study star-by-star with very high resolution in three-, four- or even six-dimensional phase space. So far, three effects have hampered these ambitions: first, our lack of accurate distance measurements to stars; second, our lack of accurate proper motions of stars; and third, our inability to see across the Galactic disk because of dust absorption. Because of these we do not yet have the solar circular speed to better than 10%, the disk scale length to better than 20%, or an accurate assessment of our own Galaxy’s rotation curve beyond the solar circle (see Olling & Merrifield 1998). We have only fairly recently become convinced of the barred nature of the Milky Way (Blitz & Spergel 1991; Weinberg 1992) and are unsure whether we live in a flocculent or grand design spiral (Quillen 2002).

The *Hipparcos* Space Astrometry Mission revolutionized our understanding of the solar neighborhood by compiling 1 milliarcsec level astrometry of 120,000 stars. Using this data Cr ez e et al. (1998) and Holmberg & Flynn (2000, 2004) measured the local matter density in the disk (the Oort limit) to be $\sim 0.1 M_{\odot} \text{pc}^{-3}$, a value that leaves little room for any significant contribution from disk dark matter. Such an explicit decomposition of baryonic and dark matter contributions to a disk potential is impossible in external galaxies. Flynn et al. (2006) used these results to estimate the local surface mass-to-light ratios (M/L) for the Galactic disk of $(M/L)_V = 1.5 \pm 0.2 M_{\odot} L_{\odot}^{-1}$ and inferred that the Milky Way is under-luminous by about 1σ with respect to the Tully–Fisher relation; if the rotation speed announced by Reid et al. (2009) is correct this discrepancy is even more significant. While these studies demonstrate the importance of large-scale, systematic Galactic studies to understanding galaxies in more detail, *Hipparcos*’ distance horizon was about 100 pc (distances of 10% accuracy) so it could not map the distribution of the mass in the Galaxy beyond the solar neighborhood.

Three innovations in observations promise to dramatically improve our understanding of the phase-space structure of our Galactic disk: (1) large-scale photometric surveys, both existing (the Two Micron All Sky Survey (2MASS) and the Sloan Digital Sky Survey) and planned (PanSTARRS and LSST), together with methods of deriving accurate photometric parallaxes for stars in these surveys (Majewski et al. 2003; Juri c et al. 2008). (2) high-precision (few to 10’s of μas) astrometry from radio observations of masers e.g., VERA

(Honma et al. 2000), VLBA (Reid 2008; Hachisuka et al. 2009) and the European VLBI Network (Rygl et al. 2008) and optical observations of stars (NASA’s SIM Lite—Space Interferometry Mission Lite and ESA’s GAIA—Global Astrometric Interferometer for Astrophysics, see Unwin et al. 2007¹; Perryman 2002); and (3) large-scale, high-resolution spectroscopic surveys, such as the ongoing Radial Velocity Experiment (RAVE; Steinmetz et al. 2006) and the SEGUE project of the Sloan Digital Sky Survey (Beers et al. 2004) as well as the planned Apache Point Observatory Galactic Evolution Experiment (APOGEE; Allende Prieto et al. 2008), HERMES instrument for the Anglo Australian Telescope and Wide Field Multi-Object Spectrograph (WFMOS) for the Gemini telescope. It is clear that any or (better yet) all of these advances will significantly improve our knowledge of the Galaxy. What is unclear is the relative contribution of each type of survey: how uncertain and/or biased will our mass estimates be if one (or more) dimensions of phase space remain unmeasured? How far across the Galactic disk do we need to probe in order to construct its rotation curve confidently? To what extent can measurement errors be compensated for by using large numbers of stars? Our study represents a first step toward addressing these questions.

Here we describe a general method to recover the underlying potential of the Galaxy from photometric, astrometric, and spectroscopic surveys of disk stars (Section 2.2). We test our method by constructing nonaxisymmetric particle disks orbiting in a given potential, simulating observations of these particles with varying degrees of accuracy, sample size, and disk coverage (Section 2.1) and examining how well the underlying potential can be measured. We present the results of applying the recovery routine to our “observed” data sets in Section 3, discuss the implications of these results for future surveys in Section 4, and summarize our conclusions in Section 5.

2. Methods

2.1. Particle Disk Realizations

This paper focuses on how astrometric determinations of the motions of disk stars in the Galaxy can best be utilized to measure the total potential in which they are moving: we neither attempt to disentangle the disk and halo contributions to the potential nor model motions perpendicular to the Galactic plane, although the methods that we describe in this paper can easily be extended to these tasks. Moreover, we do not address the use of radial velocity-only surveys. We explore the power of astrometric measurements to measure the

¹This actually presents about SIM PlanetQuest instead of SIM Lite

Galactic potential by using an approximate, parameterized kinematical model to generate a stellar sample, adding observational errors and then attempting to recover the parameters of the model.

The positions and motions of particles in our models are generated from analytical formulae derived for axisymmetric disks perturbed by spiral arms. We stress that our use of approximate analytical formula (e.g., from epicycle theory) does not compromise the validity of our results so long as the *same* approximate formulae used to generate the particle realization are used to recover the parameters of the model from observations of the realization. In other words, the tests described in this paper provide an accurate assessment of the validity of our method so long as accurate physics is used when analyzing the real data. Of course, a potential problem for applying this method—or any method based on parameterized models—is that the results may be misleading if the parameterized models are not an accurate description of the real Galaxy.

The total potential is written as a sum of axisymmetric Φ and spiral arm Φ_s terms

$$\Phi_{\text{total}} = \Phi(R) + \Phi_s(R, \phi, t) \quad (1)$$

where R is the Galactocentric radius and ϕ is the azimuthal angle in the disk, measured from the Sun–Galactic center (GC) line and increasing in the same direction as Galactic rotation.

The particles are assumed to be drawn from an underlying axisymmetric distribution of number density $\Sigma_{\text{sym}}(R)$, whose response to the spiral arm potential perturbation $\Sigma_s(R, \phi, t)$ is calculated in the linear regime, to give a total number density:

$$\Sigma = \Sigma_{\text{sym}}(R) + \Sigma_s(R, \phi, t). \quad (2)$$

The motions of the particles in the underlying potential are chosen to maintain the number density distribution: the mean radial (\bar{v}_R) and azimuthal (\bar{v}_ϕ) speeds are given by

$$\bar{v}_R = \bar{v}_{R,\text{sym}}(R) + v_{Rs}(R, \phi, t), \quad (3)$$

$$\bar{v}_\phi = \bar{v}_{\phi,\text{sym}}(R) + v_{\phi s}(R, \phi, t), \quad (4)$$

where ($\bar{v}_{R,\text{sym}}, \bar{v}_{\phi,\text{sym}}$) are the mean radial and azimuthal speeds, respectively, set by the gravitational potential of the axisymmetric disk, and ($v_{Rs}, v_{\phi s}$) are additional perturbations to the mean due to spiral structure (see Equations 14-19 below).

The formulae, adopted functional form and parameters for axisymmetric and spiral arm terms in Equations (1) - (4) are described in Sections 2.1.1 and 2.1.2, respectively. The dashed lines in Figure 1 show the results for our standard model (hereafter, the INPUT model), and the dots show the velocities for a sample of particles in the range $\phi = \pm\pi/16$ radians generated from this model without errors.

2.1.1. *Axisymmetric potential, number density and motions*

The realized disks are zero-thickness and exponential in Galactocentric radius R :

$$\Sigma_{\text{sym}}(R) = \Sigma_0 \exp\left(-\frac{R}{h}\right). \quad (5)$$

where Σ_0 is the central value and $h = 3.0$ kpc is the scale length of the disk number density.

We work in terms of a spherical mass distribution for simplicity, even though the actual mass distribution is certainly flattened, because we are only modeling the potential in the disk midplane. The combined disk and halo mass distribution is represented by a Hernquist function (of total mass $M_h = 10^{12} M_\odot$ and scale length $a = 22$ kpc, Hernquist 1990),

$$M(R) = \frac{M_h R^2}{(R + a)^2}, \quad (6)$$

where $M(R)$ is the mass enclosed within radius R . The corresponding potential is

$$\Phi(R) = \frac{-GM_h}{(R + a)}. \quad (7)$$

The circular velocity in this potential is calculated via

$$v_{\text{circ}}(R) = \sqrt{R \frac{d\Phi}{dR}} = \sqrt{\frac{GM}{R}} = \frac{\sqrt{GM_h R}}{(R + a)}. \quad (8)$$

The radial velocity dispersion is assumed to follow

$$\sigma_R^2(R) = \sigma_{R,\odot}^2 \exp\left(\frac{R_0 - R}{h_\sigma}\right), \quad (9)$$

where $\sigma_{R,\odot} = 25 \text{ km s}^{-1}$ is the radial velocity dispersion at the Sun (taken to be at $R_0 = 8$ kpc from the GC). Our potential recovery algorithm determines h_σ independently of h , i.e., it does not assume that $h_\sigma = h$. If the disk is self-gravitating, the shape of the velocity ellipsoid is independent of radius, and the disk thickness is independent of radius (as observed in external galaxies) then we expect $h_\sigma = h$ (see details in Hernquist 1993). Thus our input model assumes $h_\sigma = h = 3.0$ kpc. It is not certain that this assumption is true for the Galactic disk, since estimates for h (e.g., Ojha, Bienaymé, Robin & Mohan 1994, found $h = 2 - 2.5$ kpc for the old disk stars) and h_σ (e.g., Lewis & Freeman 1989, found $h_\sigma = 4.37 \pm 0.32$ kpc in a study of old disk K-giants) are not same.

The azimuthal velocity dispersions σ_ϕ are assigned according to epicycle theory,

$$\sigma_\phi(R) = \sigma_R \sqrt{\frac{\kappa^2}{4\Omega^2}}, \quad (10)$$

where $\Omega = v_{\text{circ}}/R$ is the angular velocity of a circular orbit at radius R and κ is the epicyclic frequency given by

$$\kappa^2(R) = \frac{\partial^2 \Phi}{\partial R^2} + \frac{3v_{\text{circ}}^2}{R^2} = \frac{GM}{R^3} + \frac{G}{R^2} \frac{dM}{dR}. \quad (11)$$

The mean azimuthal motion $v_{\phi, \text{sym}}$ due to the axisymmetric potential is given by the asymmetric drift equation,

$$\bar{v}_{\phi, \text{sym}}^2(R) = v_{\text{circ}}^2 - \sigma_{\phi}^2 + \sigma_R^2 + \frac{R}{\Sigma_{\text{sym}}} \frac{\partial(\Sigma_{\text{sym}} \sigma_R^2)}{\partial R} = v_{\text{circ}}^2 - \sigma_{\phi}^2 + \sigma_R^2 - R \sigma_R^2 \left(\frac{1}{h_{\sigma}} + \frac{1}{h} \right), \quad (12)$$

where the second equality was derived using Equations (5) and (9). The mean radial motion $\bar{v}_{R, \text{sym}}$ is zero.

2.1.2. Spiral arms

The m -armed spiral potential is of the form

$$\Phi_S(R, \phi, t) = \Phi_a(R) \cos \left[m(\phi - \Omega_p t) + c \log \left(\frac{R}{8 \text{ kpc}} \right) + \phi_0 \right] \quad (13)$$

where Φ_a is the amplitude of the spiral potential, Ω_p is its pattern speed and $k = c/R$ is the radial wave-number which is related to the pitch angle, θ , by $\cot \theta = c/m$. For the remainder of the discussion we consider the case of an $m = 2$ spiral, of amplitude $\Phi_{a2}(R) = 200(\text{km s}^{-1})^2$, $\Omega_p = 1.4 \text{ km s}^{-1} \text{ kpc}^{-1}$, pitch angle $\theta = 15^\circ$ and phase $\phi_0 = 105^\circ$. This potential perturbation would be generated by spiral arm of mass density $6.9 M_{\odot} \text{ pc}^{-2}$ (from Equation 6.30 of Binney & Tremaine 2008) or about 10% of the observed local disk surface density.

Note that these parameters are specifically chosen so that any resonances lie outside our survey region; in particular the pattern speed is much lower than typical (very uncertain) estimates of the pattern speed in the Galaxy (Debattista, Gerhard & Sevenster 2002). Moreover, with this pattern speed the entire observable disk lies inside the inner Lindblad resonance, a region in which self-consistent spiral waves normally do not propagate. This oversimplification will need to be addressed in future work.

The linear-theory prediction for the velocity response of the system to the imposed potential is given in the tight-winding or WKB approximation by (Binney & Tremaine 2008);

$$v_{Rs}(R, \phi, t) = v_{Ra}(R) \cos[m(\phi - \Omega_p t) + c \log \frac{R}{R_0} + \phi_0], \quad (14)$$

$$v_{\phi s}(R, \phi, t) = v_{\phi a}(R) \sin[m(\phi - \Omega_p t) + c \log \frac{R}{R_0} + \phi_0], \quad (15)$$

where

$$v_{Ra}(R) = \frac{m(\Omega - \Omega_p)}{\Delta} k\Phi_a F, \quad (16)$$

$$v_{\phi a}(R) = -\frac{2B}{\Delta} k\Phi_a F, \quad (17)$$

$$\Delta = \kappa^2 - [m(\Omega - \Omega_p)]^2, \quad (18)$$

and

$$B = -\frac{1}{2} \left[\frac{d(\Omega R)}{dR} \right] = -\Omega - \frac{1}{2} R \frac{d\Omega}{dR}. \quad (19)$$

In the above equations F is the reduction factor given by Equation (6-63) in Binney & Tremaine (2008) and the function $B(R)$ is equal to Oort’s B constant at $R = R_0$.

The number density perturbation due to the spiral potential of Equation (13) is given by

$$\Sigma_s(R, \phi, t) = \Sigma_a(R) \cos \left[m(\phi - \Omega_p t) + c \log \left(\frac{R}{8 \text{ kpc}} \right) + \phi_0 \right], \quad (20)$$

where the amplitude of the response number density Σ_a is given by Equation (6-59) in Binney & Tremaine (2008):

$$m(\Omega - \Omega_p)\Sigma_a + k\Sigma_0 v_{Ra} = 0. \quad (21)$$

2.1.3. Rendering and “Observing” the Particle Disks

The stellar sample generated from our particle disks simulates the collection of data by a targeted astrometric study, such as might be performed with SIM Lite. In particular, the target stars are selected based on estimated photometric parallaxes, then the trigonometric parallaxes of these targets are observed with appropriate errors. We anticipate that our results will be broadly applicable to global astrometric surveys (e.g., the GAIA mission), as well as smaller samples currently available from ground-based surveys (e.g., VERA). The error distribution function would differ in these cases, but we defer more detailed discussion of these alternative applications to Section 4.

We use the following steps to generate our simulated data.

1. The stars in the disk are generated over a radius range from $R = 0$ kpc to 25 kpc, distributed according to the number density distribution of Equation (2). These stars are viewed from a point moving (in Galactic rest-frame coordinates) with radial and azimuthal speeds $(v_{R,\text{view}}, v_{\phi,\text{view}}) = (v_{R,\text{LSR}}, v_{\phi,\text{LSR}}) = (\bar{v}_R, \bar{v}_\phi)$ at $R_0 = 8$ kpc from the GC

(i.e., at the Sun) and each star is assigned a Galactic longitude l and parallax p . Here we assume $\mathbf{v}_{\text{view}} = \mathbf{v}_{\text{LSR}}$ where \mathbf{v}_{LSR} is the velocity of the Local Standard of Rest, because the peculiar velocity of the Sun relative to the LSR is known (Dehnen & Binney 1998). The proper motion μ and line-of-sight velocity v_{los} of the stars are assigned based on (v_R, v_ϕ) drawn from Gaussians with means $(\bar{v}_R, \bar{v}_\phi)$ given by Equations (3) and (4) and dispersions (σ_R, σ_ϕ) given by Equations (9) and (10) at each position.

2. The stars' parallaxes are scattered about their true values to give observed photometric parallaxes p_{phot} by drawing from a Gaussian distribution of mean p and dispersion $\delta_{p,\text{phot}}$. This observational uncertainty is assumed to be 15% (i.e., $\delta_{p,\text{phot}} = 0.15p$) in most of the following work except in Section 3.4 (see also details in Section 3.1). This step is intended to mimic the effect of drawing a sample from a set of standard candles, with absolute magnitudes in a well-characterized range. Errors in l are negligible.
3. In our recovery algorithm, we parameterize the potential using characteristic masses $M_i \equiv M(R_i)$ defined at eight discrete radii R_i uniformly spaced from $R_1 = 4$ kpc to $R_8 = 20$ kpc (see Section 2.2.3 for details). In order to have adequate constraints on each M_i , sample stars are selected based on observed p_{phot} (i.e., including the uncertainty introduced by the distribution of absolute magnitudes of the standard candles) so that there are equal numbers of stars in the seven bins between the R_i . We impose the following additional restrictions on the sample, while retaining the constraint that there should be equal numbers of stars in each bin. (1) Sample stars are selected only between Galactocentric radii of R_1 and $R_{\text{max}} = \min(18 \text{ kpc}, R_8 - 0.17d)$, where d is the distance from the Sun. The d dependence in R_{max} is introduced to minimize the number of stars that scatter into our sample from outside our intended survey region since this could result in a systematic bias in our estimate for M_8 . The dependence is tuned to the scale of the uncertainties: $0.17d$ corresponds to the 1σ uncertainty in distance due to a 15% error in photometric parallax. (2) No sample stars have $d > 20$ kpc, to avoid stars with large distance errors. (3) Stars behind the Galactocentric circle at R_1 (i.e., $l < l_{\text{min}} = 30^\circ$ and $d > 8 \text{ kpc} \cos l_{\text{min}}$) are also excluded because of the typically strong extinction. The observed spatial distribution (i.e., using p_{phot} to find location in the disk) of a sample of stars selected in this manner from the exponential disk is shown as black dots in Figure 2. The true spatial distribution of this sample of stars is also shown as gray filled circles. Note that because these target stars are selected based on p_{phot} rather than p , some fraction of our sample actually lies outside our intended survey region.
4. The observed trigonometric parallax, proper motion and line-of-sight velocity ($p_{\text{tri}}, \mu_o, v_{\text{los},o}$) for our sample are assigned by drawing from Gaussian distributions of mean

(p, μ, v_{los}) , given in step 1 above, and dispersion $(\delta_{p,\text{tri}}, \delta_{\mu}, \delta_{\text{los}})$ where $\delta_{p,\text{tri}}$ and δ_{los} are constant and δ_{μ} depends on $\delta_{p,\text{tri}}$ (see details in Section 3.1). This step is intended to mimic a targeted astrometric mission with ground-based spectroscopic follow-up, observing the sample stars with integration times tailored to achieve a constant accuracy. The faintest (i.e., most distant and smallest p) stars in any sample may have more accurate photometric parallaxes than trigonometric parallaxes.

2.2. Recovering the Underlying Potential

The recovery program uses a Markov Chain Monte Carlo approach (MCMC, as described in Gilks, Richardson & Spiegelhalter 1996; Verde et al. 2003 and summarized below in Section 2.2.1) to find the maximum and the shape of the likelihood function

$$L(\mathbf{x}) = \prod_{i=1}^N P(p_{\text{tri}}^i, \mu_{\text{o}}^i, v_{\text{los,o}}^i | p_{\text{phot}}^i, l^i, \mathbf{x}), \quad (22)$$

for a sample of size N as the parameters of the model \mathbf{x} are varied. Here $P(p_{\text{tri}}^i, \mu_{\text{o}}^i, v_{\text{los,o}}^i | p_{\text{phot}}^i, l^i, \mathbf{x})$ is the conditional probability (derived in Section 2.2.2) of observing a star to have trigonometric parallax, proper motion and line-of-sight velocity $(p_{\text{tri}}, \mu_{\text{o}}, v_{\text{los,o}})$, given its observed photometric parallax p_{phot} and Galactic longitude l , and underlying Galaxy model parameters \mathbf{x} (see Section 2.2.3).

P represents the conditional probability of observing a star’s kinematical properties at a particular position in the disk. Hence, although we need to have an appropriate model of the intrinsic stellar spatial distribution from which we are selecting the sample (in order to understand the likelihood of finding a star of given p_{phot} and p_{tri} in the initial random survey), we have complete freedom in specifying how we select the stars in our targeted sample. This means we can choose to distribute our tracers to regions of the disk that we are most interested in resolving. In our case (as noted in Section 2.1.3), we select equal numbers of stars with observed Galactocentric radii (based on the photometric parallax) in each of the seven bins between the R_i , rather than simply taking a random sample, and this allows us to explore the outer disk in greater detail.

2.2.1. The Markov Chain method

In a single step of a MCMC run, the likelihood $L_{i,\text{prop}}$ (Equation 22) is evaluated for the model parameters $\mathbf{x}_{i,\text{prop}}$ proposed at step i in a chain and compared with L_{i-1} from the

previous step. If $L_{i,\text{prop}} > qL_{i-1}$, for a random number q between 0 and 1, the proposed parameters will be adopted for this step ($\mathbf{x}_i = \mathbf{x}_{i,\text{prop}}$). Otherwise the parameters from the previous step ($\mathbf{x}_i = \mathbf{x}_{i-1}$) are kept. Proposed parameters for the next step (\mathbf{x}_{i+1}) are generated by adding a vector of small changes to \mathbf{x}_i . These steps are accumulated until they satisfy the convergence criteria outlined in Verde et al. (2003).

The beauty of the MCMC method is that the distribution of the accepted steps follows the shape of the likelihood function in parameter space. This property of the method means that the chains of steps themselves can be exploited in two ways: first they can be used to derive the optimal directions and sizes of steps for exploring parameter space (i.e., to get better acceptance ratios and faster convergence); and second, they can be used to determine best values and confidence intervals for each parameter.

In this work, a “test” MCMC is first run with step sizes for parameter changes estimated from simple intuition. The covariance matrix of these preliminary chains is then constructed, and the eigenvalues and eigenvectors of the matrix are used to estimate optimal size and direction of parameter vectors of the steps made in the following actual MCMC runs. This refinement is particularly important when the parameters have strong correlations (see Section 3).

The “best” values of parameters presented in all figures and tables are taken to be the mean \mathbf{x} from the chains, weighted by the likelihood. The $1\text{-}\sigma$ error bars represent 68% confidence intervals.

2.2.2. Estimating the likelihood of a given parameter set

The likelihood in Equation (22) is the product of factors $P(p_{\text{tri}}, \mu_o, v_{\text{los},o} | p_{\text{phot}}, l, \mathbf{x})$ for each star in the sample, which is the conditional probability of making observations of trigonometric parallax p_{tri} , proper motion $\mu = \mu_o$ and line-of-sight velocity $v_{\text{los}} = v_{\text{los},o}$ given an observed photometric parallax p_{phot} , along Galactic longitude l ,

$$\begin{aligned} P(p_{\text{tri}}, \mu_o, v_{\text{los},o} | p_{\text{phot}}, l, \mathbf{x}) &= \frac{P(p_{\text{phot}}, p_{\text{tri}}, \mu_o, v_{\text{los},o} | l, \mathbf{x})}{P(p_{\text{phot}} | l, \mathbf{x})} \\ &= \frac{P(p_{\text{phot}}, p_{\text{tri}}, \mu_o, v_{\text{los},o} | l, \mathbf{x})}{\int_0^\infty dp_{\text{tri}} \int_{-\infty}^\infty d\mu_o \int_{-\infty}^\infty dv_{\text{los},o} P(p_{\text{phot}}, p_{\text{tri}}, \mu_o, v_{\text{los},o} | l, \mathbf{x})}. \end{aligned} \quad (23)$$

The full probability distribution can be derived from the phase-space distribution function $f_{\mathbf{x}}$ which is the number of stars per unit velocity and per unit parallax, given by

$$f_{\mathbf{x}}(p, v_{\text{tan}}, v_{\text{los}}, l) = f'_{\mathbf{x}}(p, v_{\text{tan}}, v_{\text{los}}, l)V(p) \quad (24)$$

where $V(p)$ is the volume per unit parallax at p ($\propto p^{-4}$ in three-dimensional space and $\propto p^{-3}$ for our zero-thickness disk), and $f'_{\mathbf{x}}$ is the number of stars per unit volume of phase space predicted by the model with parameters \mathbf{x} :

$$f'_{\mathbf{x}}(p, v_{\tan}, v_{\text{los}}, l) = \Sigma(p, l)U_{\mathbf{x}}(v_R, v_{\phi}). \quad (25)$$

In the above equation $\Sigma(p, l)$ is the number density of stars per unit area at (p, l) given by Equation (2) and $U_{\mathbf{x}}$ is the number of stars per unit velocity predicted from the model parameters \mathbf{x} at position (p, l) given by

$$U_{\mathbf{x}}(v_R, v_{\phi}) = g(v_R, \bar{v}_{R,\mathbf{x}}, \sigma_{R,\mathbf{x}})g(v_{\phi}, \bar{v}_{\phi,\mathbf{x}}, \sigma_{\phi,\mathbf{x}}). \quad (26)$$

Here $g(y, \bar{y}, \sigma)$ denotes the value at y of a Gaussian distribution with mean \bar{y} and dispersion σ^2 and the quantities $(\bar{v}_{R,\mathbf{x}}, \bar{v}_{\phi,\mathbf{x}})$ and $(\sigma_{R,\mathbf{x}}^2, \sigma_{\phi,\mathbf{x}}^2)$ are the mean velocity and velocity dispersion at parallax p and longitude l from the model with parameters \mathbf{x} , given by Equations (3), (4), (9), and (10) respectively. Finally, $(v_{\tan} = \mu/p, v_{\text{los}})$ can be transformed to (v_R, v_{ϕ}) for given (p, l) , v_{view} and R_0 .

In our experiment, we first observe p_{phot} for a random disk sample, with an error distribution $\epsilon(p_{\text{phot}}|p) = g(p_{\text{phot}}, p, \delta_{p,\text{phot}})$ about p . The distribution in (p, p_{phot}) of stars is given by

$$\Sigma(p, l)\epsilon(p_{\text{phot}}|p)V(p). \quad (27)$$

A subset of these stars is selected for our sample, with specified distribution $N_{\text{sample}}(p_{\text{phot}}, l)$ along a given line of sight, which can be related to the selection function, $S(p_{\text{phot}}, l)$ (i.e., the probability of including a star in the survey at (p_{phot}, l)) by

$$N_{\text{sample}}(p_{\text{phot}}, l) = S(p_{\text{phot}}, l) \int_0^{\infty} \Sigma(p, l)\epsilon(p_{\text{phot}}|p)V(p)dp. \quad (28)$$

The total number of stars in the sample N is given by summing the number of stars toward l ,

$$N_l = \int_0^{\infty} N_{\text{sample}}(p_{\text{phot}}, l)dp_{\text{phot}}, \quad (29)$$

and along all adopted lines of sight.

Hence the full distribution of properties of the sample will depend on its intrinsic distribution in phase-space $f_{\mathbf{x}}$, filtered by $S(p_{\text{phot}}, l)$ and convolved with appropriate error distributions for the remaining observables, $\epsilon(p_{\text{tri}}|p) = g(p_{\text{tri}}, p, \delta_{p,\text{tri}})$, $\epsilon(\mu_{\text{o}}|\mu) = g(\mu_{\text{o}}, \mu, \delta_{\mu})$ and $\epsilon(v_{\text{los,o}}|v_{\text{los}}) = g(v_{\text{los,o}}, v_{\text{los}}, \delta_{v_{\text{los}}})$ (as outlined in Section 2.1.3). The probability of finding a star in the survey is given by

$$P(p_{\text{phot}}, p_{\text{tri}}, \mu_{\text{o}}, v_{\text{los,o}}|l, \mathbf{x})$$

$$\begin{aligned}
&= \frac{S(p_{\text{phot}}, l)}{N_l} \int_0^\infty dp \int_{-\infty}^\infty \frac{d\mu}{p} \int_{-\infty}^\infty dv_{\text{los}} f_{\mathbf{x}}(p, \mu/p, v_{\text{los}}, l) \epsilon(p_{\text{tri}}|p) \epsilon(p_{\text{phot}}|p) \epsilon(\mu_o|\mu) \epsilon(v_{\text{los},o}|v_{\text{los}}) \\
&= \frac{S(p_{\text{phot}}, l)}{N_l} \int_0^\infty \Sigma(p, l) V(p) \epsilon(p_{\text{tri}}|p) \epsilon(p_{\text{phot}}|p) P_{p,\mu,v_{\text{los}}}(p, \mu_o, v_{\text{los},o}) dp,
\end{aligned} \tag{30}$$

where

$$P_{p,\mu,v_{\text{los}}}(p, \mu_o, v_{\text{los},o}) = \int_{-\infty}^\infty \int_{-\infty}^\infty U_{\mathbf{x}}(\mu/p, v_{\text{los}}) \epsilon(\mu_o|\mu) \epsilon(v_{\text{los},o}|v_{\text{los}}) \frac{d\mu}{p} dv_{\text{los}}. \tag{31}$$

Substituting in Equation (23) gives

$$\begin{aligned}
P(p_{\text{tri}}, \mu_o, v_{\text{los},o}|p_{\text{phot}}, l, \mathbf{x}) &= \frac{P(p_{\text{phot}}, p_{\text{tri}}, \mu_o, v_{\text{los},o}|l, \mathbf{x})}{P(p_{\text{phot}}|l, \mathbf{x})} \\
&= \frac{\int_0^\infty \Sigma(p, l) V(p) \epsilon(p_{\text{tri}}|p) \epsilon(p_{\text{phot}}|p) P_{p,\mu,v_{\text{los}}}(p, \mu_o, v_{\text{los},o}) dp}{\int_0^\infty dp_{\text{tri}} \int_{-\infty}^\infty d\mu_o \int_{-\infty}^\infty dv_{\text{los},o} \int_0^\infty \Sigma(p, l) V(p) \epsilon(p_{\text{tri}}|p) \epsilon(p_{\text{phot}}|p) P_{p,\mu,v_{\text{los}}}(p, \mu_o, v_{\text{los},o}) dp}
\end{aligned} \tag{32}$$

Note that this expression is independent of our sample selection function $S(p_{\text{phot}}, l)/N_l$: our analysis method leaves us free to choose a sample with arbitrary properties without biasing the results. Also, in the limit of negligible errors in the photometric parallax (i.e., $\epsilon(p_{\text{phot}}|p) = \delta(p_{\text{phot}} - p)$), Equation (32) simplifies to:

$$P(p_{\text{tri}}, \mu_o, v_{\text{los},o}|p_{\text{phot}}, l, \mathbf{x}) = \epsilon(p_{\text{tri}}|p_{\text{phot}}) P_{p,\mu,v_{\text{los}}}(p_{\text{phot}}, \mu_o, v_{\text{los},o}) \tag{33}$$

and our approach becomes insensitive to the underlying disk surface density distribution.

2.2.3. Parameterizing the OUTPUT model

The model distribution function $f_{\mathbf{x}}$ (see Equation 24) is fully specified by the spatial number density, mean velocities and velocity dispersions of stars as a function of position in the disk.

Our OUTPUT model can represent observations of axisymmetric motions using a total of 12 free parameters (11 free parameters when we fix R_0) to describe both $f_{\mathbf{x}}$ and the transformation from physical to observed coordinates: (1) h —the scale length of the Galactic disk given in Equation (5); (2) $\sigma_{R,\odot}$ and h_σ (assuming the functional form for the radial velocity dispersion given in Eq. 9); (3) the masses M_i ($i = 1, 2, \dots, 8$) within Galactic radius, R_i (from which the mass and its derivative $\partial M/\partial R$ at any radius are found using cubic spline interpolation); and (4) R_0 . We also analyze the sample assuming a known value $R_0 = 8$ kpc in the following sections because we anticipate that it will be well-constrained by other observations (e.g., adaptive optics observations of stars around the black hole at the

Galactic center; Eisenhauer et al. 2003). The effect of allowing R_0 to be a free parameter or fixed is shown in Section 3.2 and 3.5.

All other quantities needed are derived from these parameters using the expressions given in Section 2.1.1.

Describing the spiral arms assuming $m = 2$ requires an additional four parameters: the constant c which is related to the radial wave number, $k = c/R$; the pattern speed Ω_p ; the arm’s phase ϕ_0 and the amplitude of the spiral potential, Φ_a . The perturbations to the mean velocities and number density are calculated using Equations (14), (15), and (20).

The 16 free parameters are listed in Table 1, along with the INPUT values from which we derived our observed sample.

3. Results

In this section, we explore the accuracy of results recovered by applying the MCMC method to simulated observations of our disk model, with INPUT parameters given in Table 1. For our standard sample, we look at disk M-giant stars, observed with fixed astrometric accuracies, as an example of a plausible near-future experiment that might be performed by a mission such as SIM Lite (see Section 3.1). M-giants are evolved, metal-rich stars and therefore typically relatively young (several Gyrs in age); this makes them good dynamical tracers of the mean disk potential. We then go on to examine how our results depend on sample size (Section 3.2), trigonometric and photometric accuracy (Sections 3.3 and 3.4) and disk coverage (Section 3.5).

3.1. The standard sample

Our photometric sample is assumed to be composed of disk M-giants selected using the infra-red color in the 2MASS catalog. We assume that the intrinsic scatter in the absolute magnitudes of the M-giants around a mean of $M_V = -2$ would result in a photometric parallax error of 15%, i.e., $\delta_{p,\text{phot}} = 0.15p$ (as estimated by Majewski et al. 2003). Note that this scatter is in part due to metallicity differences (Chou et al. 2007), and measuring the metallicity to about 0.3 dex would allow a parallax accuracy as good as $\sim 10\%$.

We select ~ 850 stars from our simulated M-giant survey to follow the distribution outlined in Section 2.1.3, and “observe” them with a trigonometric parallax accuracy of $\delta_{p,\text{tri}} = 10 \mu\text{as}$. With these parameters, the point at which photometric rather than trigono-

metric parallaxes became more accurate would be at $p \sim 67 \mu\text{as}$ (~ 15 kpc). The proper motion accuracy is expected to scale as

$$\delta_\mu = [0.235 + 0.634 \times \delta_{p,\text{tri}}(\mu\text{as})] \mu\text{as yr}^{-1} \quad (34)$$

from the SIM Global Astrometry Time Estimator². We assume a constant error in the line-of-sight velocity $\delta_{v,\text{los}}=1 \text{ km s}^{-1}$ can be achieved from ground-based spectroscopic observations.

Figure 1 illustrates the results of applying the MCMC recovery routine to this standard sample, with the analytical estimates constructed from INPUT and recovered OUTPUT parameters (listed in Table 1) shown as dashed and solid lines, respectively. The best fit values at interpolated points are plotted as filled circles, with $1\text{-}\sigma$ error bars estimated directly from the distribution of parameters in the MCMC. The figure indicates that, with this level of accuracy, we can recover the mass distribution between 4 and 20 kpc to within $\sim 2\%$ using a sample size $\lesssim 10^3$.

Figure 3 shows the full likelihood distribution of parameters. There are strong correlations between (a) M_i 's and R_0 : due to the relation $M = v_{\text{circ}}^2 R G^{-1}$; (b) M_i 's at large R : all M_i correlate with R_0 simultaneously; (c) c and ϕ_0 : they define the phase of the spiral arms by Equations (14) and (15); (d) Φ_a and Ω_p : the amplitude of the mean velocity in the spiral arms is related to them by Equations (14) and (15). As noted in Section 2.2.1, the steps in the MCMC were optimized using a preliminary run to take account of these correlations prior to our production runs. However, these contours in correlated parameters become longer and banana-shaped for small N , large observational errors and narrow coverage of samples in space (e.g., small ϕ_{max} defined in Section 3.5), and under these conditions the MCMC can fail to converge.

In order to check for systematic biases in our methods as well as confirm the size of our error estimates, Figure 4 repeats the middle left panel of Figure 1 for 10 runs of the MCMC (gray dots) applied to 10 independent samples of simulated stars. The sizes of the errors are not shown, but are similar to those shown in Figure 1. Open circles and error bars indicate the mean ΔM_i of the 10 runs and its estimated 1σ error, and the solid line is the spline interpolation of the mean ΔM_i . Only two of the means lie (a little) more than 1σ away from the INPUT model ($\Delta M_i = 0$) and thus the scatter is consistent with the estimated statistical error of the means estimated from the 10 runs. In addition, the standard deviation of the OUTPUT mass parameters from their INPUT values, $sdev = (0.20 \pm 0.02) \times 10^{10} M_\odot$ (calculated for the 10 runs over all eight points) is consistent with the mean of the errors estimated from the MCMC $\bar{\delta}_M = (0.21 \pm 0.004) \times 10^{10} M_\odot$. Overall, these comparisons

²<http://mscws4.ipac.caltech.edu/simtools/portal/login/normal/1?>

validate the error estimates derived from the MCMC (i.e., $sdev \approx \bar{\delta}_M$) as well as the success of our method in modeling the adopted observing strategy.

Note that the results in this section also confirm that this method does not require knowledge of the true spatial distribution of our sample stars — the algorithm we chose to pick the sample does not enter into the analysis. Indeed, the gray points in Figure 2 show that the intrinsic scatter in M-giant absolute magnitudes means that some of our sample lies outside of our intended survey region, $R = R_8 = 20$ kpc, where the last of our mass parameters is defined. A small systematic bias is apparent if we relax our requirement that a star’s position defined by its photometric parallax lies well within this outer radius limit (recall, $R_{\max} = \min(18 \text{ kpc}, R_8 - 0.17d)$) and instead include stars whose observed p_{phot} places them all the way out to $R = 20$ kpc. Our choice of keeping our samples to within $R = 18$ kpc keeps this bias negligible.

In each of the following subsections (and Figures 5 - 8), we repeat the comparison of $sdev$ and $\bar{\delta}_M$ to check for systematic biases that may become apparent for samples observed under different conditions.

3.2. Dependence on N

Figure 5 plots $sdev$ and $\bar{\delta}_M$ as a function of the number of stars observed N , with all other properties of the sample maintained at their standard values (see Table 2 for full listing of errors on all parameters). The agreement of the black filled and gray open symbols demonstrates both the lack of systematic biases in our recovery algorithm and the success of the MCMC error estimates. The solid lines, representing the power law

$$\left(\frac{\delta_M}{10^9 M_\odot} \right) = 1.7(2.7) \times \sqrt{\frac{500}{N}} \quad (35)$$

for fixing (fitting) R_0 , confirm the expected $N^{-1/2}$ scaling of errors. The uncertainties in parameters for the case of fitting R_0 are increased only by order unity compared to the case of fixing R_0 . The uncertainty in R_0 as a function of N is given by the formula

$$\left(\frac{\delta_{R_0}}{\text{kpc}} \right) = 0.16 \times \sqrt{\frac{500}{N}}. \quad (36)$$

3.3. Dependence on $\delta_{p,\text{tri}}$

Figure 6 and Table 3 summarize the results of repeating the analysis of Section 3.1 for MCMC runs based on the standard sample but with varying trigonometric parallax errors $\delta_{p,\text{tri}}$ (and related proper-motion accuracies—see Equation 34).

The figure indicates that trends of the uncertainty δ_M with $\delta_{p,\text{tri}}$ can be roughly split into three regimes. As might be expected, δ_M increases with $\delta_{p,\text{tri}}$ for $\delta_{p,\text{tri}}$ less than $\sim 10 \mu\text{as}$ and $\delta_{p,\text{tri}}$ greater than $\sim 200 \mu\text{as}$. However, δ_M is almost constant for $\delta_{p,\text{tri}}$ in the range $10 - 200 \mu\text{as}$. This behavior can be understood by considering the importance of the sources of observational error in each of these three regimes.

For $\delta_{p,\text{tri}} < 10 \mu\text{as}$ the trigonometric parallax is more accurate than the photometric parallax for most of the stars in the sample (those with $p < 67 \mu\text{as}$ and distances less than 15 kpc), while the proper-motion ($\sim 6 \mu\text{as yr}^{-1}$, corresponding to $v_{\text{tan}} < 1 \text{ km s}^{-1}$ at < 20 kpc) and line-of-sight velocity accuracies (1 km s^{-1}) are much smaller than the scales of the velocity dispersions ($\sim 25 \text{ km s}^{-1}$) of the population that they are trying to measure. Hence, the uncertainty scales with $\delta_{p,\text{tri}}$

For $10 \mu\text{as} < \delta_{p,\text{tri}} < 200 \mu\text{as}$, the photometric parallax—held constant at 15%—provides stronger constraints on the results than the trigonometric parallax, and the proper motion and velocity accuracies are still too small to increase δ_M .

For $\delta_{p,\text{tri}} > 200 \mu\text{as}$, while the photometric parallax still provides 15% constraints on the distances to stars, the proper-motion error is increasing with $\delta_{p,\text{tri}}$ beyond 0.21 mas yr^{-1} , or $\sim 10 \text{ km s}^{-1}$ for stars at 10 kpc. Hence, the accuracy with which the motions of distant stars can be determined is of the same order as their velocity dispersion and this now limits the accuracy with which the mass can be measured.

We will discuss the implications of these trends for future surveys in Section 4.

The overlap of the black and gray points in Figure 6 once again confirms the lack of systematic biases in our recovery algorithm.

3.4. Dependence on $\delta_{p,\text{phot}}$

We assume 15% photometric parallax accuracy in most of this work, i.e., $\delta_{p,\text{phot}} = 0.15p$. We show the dependence of the accuracy of parameter estimates on various parallax accuracies, $\delta_{p,\text{phot}} = 0.1p, 0.15p$ and $0.2p$ for $\delta_{p,\text{tri}} = 10$ and $1000 \mu\text{as}$ in Figure 7 and Table 4.

In general, we find that the mean error on parameters *decreases* slightly as $\delta_{p,\text{phot}}$ increases for $\delta_{p,\text{tri}} = 10 \mu\text{as}$, while the mean error is independent of $\delta_{p,\text{phot}}$ for $\delta_{p,\text{tri}} = 1000 \mu\text{as}$.

This counter-intuitive result—clearly in contradiction with the expectation that the errors on estimates should decrease as measurements become more accurate—can be attributed to the different nature of the samples in each case. Since the stars are selected using their photometrically estimated distances, d_{phot} (see Section 2.1.3), the spatial distribution of the true positions of stars changes with $\delta_{p,\text{phot}}$: the larger $\delta_{p,\text{phot}}$, the more the distribution of true distances is determined by the parameters of the disk rather than the parameters of the survey.

For samples that are then observed with $\delta_{p,\text{tri}} = 10 \mu\text{as}$, the trigonometric parallax is more accurate than the photometric parallax for the majority of the stars ($d < 15 \text{ kpc}$). Hence, even if $\delta_{p,\text{phot}}$ increases, the accuracy of the dominant distance estimates in the analysis remains the same, while the area of the disk explored by the selected stars goes up and the net effect is an improvement in the errors on the parameters.

For the same samples observed with $\delta_{p,\text{tri}} = 1000 \mu\text{as}$, the photometric parallax is more accurate than the trigonometric parallax for the majority of the stars ($> 100\text{pc}$). Now both the errors in the distance estimates and disk coverage increase with $\delta_{p,\text{phot}}$, and these effects exert competing influences on the parameter estimates. Hence the size of uncertainties on the parameters is largely independent of $\delta_{p,\text{phot}}$.

The only exception to these trends in errors is for the disk scale length h , where the mean error decreases as $\delta_{p,\text{phot}}$ increases for both values of $\delta_{p,\text{tri}}$. This can be explained by recalling that the number density distribution only contributes to the likelihood function if the scattering of stars due to the uncertainty of p_{phot} is sufficiently large to sense the shape of the number density, by which the likelihood function is weighted—in the idealized case of zero errors, the method cannot constrain h at all (see Section 2.2.2 and Equations 23-30). This effect compounds rather than competes with the trend due to changing sample distributions as $\delta_{p,\text{phot}}$ changes for both values of $\delta_{p,\text{tri}}$.

To check how the results would be affected by systematic errors, we ran our analysis on samples constructed assuming photometric parallaxes that were 10% smaller or larger than the true parallax in addition to the random errors. The resultant M_i are systematically overestimated and underestimated by up to 10%, respectively. The parameters Φ_a and h are also biased by 30%-50%.

3.5. Dependence on disk coverage and knowledge of R_0

To check how the spatial distribution of our sample stars affects our recovery, we ran the MCMC for samples chosen with various values of ϕ_{\max} , the maximum absolute azimuthal angle of stars in the sample around the GC, i.e., $|\phi| < \phi_{\max}$ (see Figure 2). Here the angles ϕ of sample stars are estimated using l and p_{phot} . In all previous analyses we have not restricted ϕ (except that $\phi_{\max} \sim 133^\circ$ in practice in our sample selection as seen in Figure 2). The results are shown in Table 5 (with sample sizes $N = 850$ and $N = 2000$) and summarized in Figure 8 (for $N = 2000$). As might be anticipated, the smaller the disk coverage (smaller ϕ_{\max}), the bigger the uncertainty of parameters—it is harder to be certain of the nonaxisymmetric features in the disk without a global view. For our particular disk model, it was necessary to cover more than $\phi_{\max} = 60^\circ$ to recover parameters effectively. If ϕ_{\max} was sufficiently small, the MCMC failed to converge altogether (e.g., if $\phi_{\max} \leq 20^\circ$ and $\leq 10^\circ$ with $N = 850$ and 2000 , respectively, when R_0 is fitted).

Figures 5 and 8 and Tables 2 and 5 illustrate the results of experiments both for the case of fitting the distance R_0 to the GC and the case of fixing $R_0 = 8$ kpc assuming an accurate assessment of R_0 has been made from other sources (e.g., Eisenhauer et al. 2003). If the disk is surveyed globally (i.e., for large ϕ_{\max}), R_0 can be recovered with a few percent accuracy (see Table 2 and 5) using the adopted samples, and the uncertainties in other parameters are increased only by order unity compared to the case of fixing R_0 . However, for $\phi_{\max} < 60^\circ$ the uncertainty in R_0 and all other parameters increases even more dramatically with ϕ_{\max} compared to the examples where R_0 was fixed.

4. Discussion: implications for near-future surveys

4.1. Astrometric surveys

4.1.1. NASA’s Space Interferometry Mission (SIM) Lite

SIM Lite is a planned astrometric satellite using an optical interferometer, which will yield parallax errors as small as $4 \mu\text{as}$ in wide angle mode. SIM Lite observes a parallax and a proper motion by repeatedly pointing at a target star and integrating as long as is necessary to get the required accuracy. For example, Figure 9 shows the expected mission time for stars requiring accuracies $\delta_{p,\text{tri}} = 8, 10, 20$ and $100 \mu\text{as}$ observed in wide angle mode up to the limiting magnitude $V = 20$.³

³<http://mscws4.ipac.caltech.edu/simtools/portal/login/normal/1?>

Observers are allocated a specific amount of time to design their own experiments. Hence, for any disk study it is vital to find the optimal number, spatial coverage and required trigonometric accuracies of target stars to recover the Galactic mass distribution most effectively. Figure 6 and Table 3 suggest that the uncertainties in our mass estimates are only weakly dependent on $\delta_{p,\text{tri}}$ in the 10-100 μas regime. On the other hand, Figure 5 and Table 2 suggests that the uncertainty scales as $\sqrt{1/N}$ (as given in Equations 35 and 36). These results imply that our best strategy for studies of the mass distribution in the Galactic disk using SIM Lite (assuming that the astrometric errors are indeed statistical, not systematic) is to choose as large a sample as possible within the given observing time rather than using the time to get the best astrometric accuracies for a smaller number of targets.

In principle, the number of stars observed by SIM Lite could be maximized by looking only at objects brighter than some limiting magnitude, V_1 . In order to make a realistic assessment of the extent to which such a magnitude limit would compromise our spatial coverage we need to also account for extinction in the disk plane. G. Zasowski, private communication, found typical V -band extinctions in the Galactic disk to be: $A_V \sim (1.5 - 8) \times d\text{kpc}^{-1}$ at $|l| < 15^\circ$, $A_V \sim 0.8 \times d\text{kpc}^{-1}$ at $|l| = 60^\circ$ and $A_V \sim 0.68 \times d\text{kpc}^{-1}$ at $|l| = 90^\circ$ and 180° . With our small sample size ($N \sim 1000$), we assume we can restrict our attention to stars that can be observed in low-extinction windows. Hence we adopt the lowest value, $A_V \sim 1.5 \times d\text{kpc}^{-1}$ for $|l| < 15^\circ$. For $|l| > 15^\circ$, the typical values are linearly interpolated in l , and a fixed fraction $A_{V,\text{win}}/A_{V,\text{typ}}$ of the estimated extinction is used. Figure 10 illustrates the spatial coverage attainable for M-giants brighter than $V_1 = 16/18/20$ and with $A_{V,\text{win}}/A_{V,\text{typ}} = 0.5$ (left-hand panel) and 0.8 (right-hand panel). While the extinction keeps us from seeing entirely across the Galactic disk in all cases, the requirement that $\phi_{\text{max}} > 60^\circ$ in order to account for disk asymmetries (see Section 3.5) is still met, at least at small radii.

Table 6 shows the number of M-giant stars that could be observed by SIM Lite within an allocation of 240 hr (motivated by the typical sizes of Key Project proposals for SIM PlanetQuest, the predecessor mission to the SIM Lite mission, which is similar, but based on a modified instrument architecture) for various V_1 and $A_{V,\text{win}}/A_{V,\text{typ}}$, adopting the strategy outlined in previous sections of sampling equal numbers of stars in the 7 radial bins between the R_i in our model (see details in Section 2.1.3). The blank entries in the table correspond to cases where one or more of the radial bins contained no stars. Indeed, while the brighter limiting magnitudes do allow more stars to be observed (i.e., larger N), the outer radial bins in these cases either contain no stars, or are only populated over a small range in ϕ .

Overall, we find that the optimal sample has $N \sim 1000$, $V_1 = 18$ and $\delta_{p,\text{tri}} = 100\mu\text{as}$. Table 7 illustrates this by showing the uncertainty $\bar{\delta}_M$ for samples with $\delta_{p,\text{tri}} = 100\mu\text{as}$ and

various V_l . Even for the worst case of $A_{V,\text{win}}/A_{V,\text{typ}} = 1.0$, the masses can be constrained with an uncertainty of $\bar{\delta}_M = 0.31 \times 10^{10} M_\odot$, which corresponds about 2% – 4% accuracy at $R = 6 - 20$ kpc.

4.1.2. ESA's GAIA satellite

Unlike SIM Lite, GAIA is an all-sky survey satellite, where each star brighter than $V = 20$ is observed for the same amount of time. Concentrating again on the M-giants, this limiting magnitude means that the GAIA catalog will contain the stars in the disk as shown in Figure 10, although they will not be distributed uniformly in Galactocentric radius (because of the disk's intrinsic density gradient) and the variation of extinction along different lines of sight means that the depth of the sample will not be constant. In addition, the fainter stars will have less accurate astrometric measurements than the brighter ones ($\delta p_{\text{tri}} = 21 \mu\text{as}$ for $V = 15$ and $275 \mu\text{as}$ for $V = 20$, with the corresponding proper-motion accuracies of $11 \mu\text{as yr}^{-1}$ and $145 \mu\text{as yr}^{-1}$ ⁴).

Figure 6 suggests that the target proper motion accuracies (better than $\sim 100 \mu\text{as yr}^{-1}$) are at the appropriate level to accurately assess the kinematical properties of disk stars when coupled with a photometric distance estimate. Nor do we expect the non-uniformity in the sample to introduce biases in results as our method is independent of the spatial distribution of the target stars. The gradient in the disk density coupled with the magnitude-limited nature of the survey means that the outer parts of the disk will be much more sparsely sampled and with larger error bars on the observations than the inner parts, so uncertainties in the mass estimates at large Galactocentric radii will increase correspondingly. In addition, since GAIA, like SIM, works in the optical, significant coverage beyond the Galactic center may be impossible due to extinction effects. However, these uncertainties can perhaps be offset by the sheer number of stars in the catalog. For example, the 2MASS catalog contains millions of M-giant candidates (i.e., in the color range $0.95 < J - K < 1.2$) brighter than $K = 14$ (corresponding to $V = 18$) within 10 deg of the Galactic plane. While there will be significant contribution by bulge stars in this sample for Galactic longitudes $|l| < 10^\circ$, they could be accounted for by adjusting the model to include this extra component. This argument assumes that the astrometric errors in GAIA are mainly statistical; given samples of this size, the biggest uncertainty with GAIA may be how large N can be before systematic errors begin to dominate the error budget. Combining the GAIA analysis with results from surveys that can fully cover the extent of the disk (e.g., SIM Lite; see Section 4.1.1) with

⁴http://www.rssd.esa.int/index.php?project=GAIA&page=Info_sheets_overview

well-characterized systematics (e.g., VERA; see Section 4.1.3) should yield a global picture of the mass distribution within the Galactic disk.

4.1.3. Radio VLBI arrays

VERA (Honma et al. 2000), VLBA (Reid 2008; Hachisuka et al. 2009), and EVN (Rygl et al. 2008) are radio VLBI arrays that are conducting $\sim 10\mu\text{as}$ astrometric observations for water and/or methanol masers. Compared to our M-giant sample, water masers have the advantage as targets that most of them lie in star-forming regions very close to the Galactic plane. Hence they have rather lower velocity dispersion and fewer sources may be needed to accurately trace the rotation curve (and mass distribution). A possible disadvantage is that star-forming regions and therefore the maser targets are generated in spiral arms and thus tend to be found in a narrow range of azimuthal phases relative to the arms. In this case there may be larger uncertainties in and strong covariances between some of the parameters. Another disadvantage of the masers formed in young star-forming regions is that these targets may not yet be dynamically homogenized to the disk, and so their motions may reflect the particular dynamics of their particular star-forming region, including such things as a vertex deviation, or other peculiar motions.

The most exciting property of these samples is that they are already being produced. For example, 18 masers with parallax errors 6-80 μas by VLBA and VERA are already in the literature (Reid et al. 2009), and VERA is expected to observe approximately 1,000 such sources over the next 10 years. This sample will have observational error properties very similar to those assumed for our standard sample (Section 3.1), except that photometric parallaxes are not available. Unlike our proposed M-giant survey, the distribution of the sources (mostly star-forming regions and some Mira variables) cannot be chosen arbitrarily, so the disk will not be uniformly sampled—in particular, water masers are more rare at large Galactocentric radii (> 10 kpc) and it may be hard to achieve full disk coverage. However, our results (e.g., Figure 6) suggest that a sample of this size and level of accuracy could provide strong constraints on the mass distribution in the inner Galaxy.

In addition to representing a significant step forward in measuring the Milky Way’s rotation curve, these observations can serve as a vital cross check for future satellite surveys that rely on more sophisticated technology and hence may be more prone to unanticipated systematic biases. Furthermore, these radio VLBI observations do not suffer from dust extinction that the optical astrometry satellites GAIA and SIM Lite will.

4.2. Spectroscopic surveys

High-resolution multi-object spectrographs are also currently under development. For example, the Apache Point Observatory Galactic Evolution Experiment (APOGEE—part of the Sloan Digital Sky Survey III project) will carry out a massive radial velocity survey starting in 2011. APOGEE will use a 300 fiber near-infrared (H-band) spectrograph with $R = 22,500 - 25,000$ to measure radial velocities to better than 0.5 km s^{-1} for more than 10^5 stars predominantly across the bulge and disk. The survey will take advantage of the low reddening in the near-infrared to reach stars throughout the Galactic disk and exploit the high resolution to make accurate estimates of spectroscopic parallaxes. Our results from Section 3.3 indicate that coupling these derived spectroscopic parallaxes with proper-motion measurements accurate to only $\sim 1 \text{ mas yr}^{-1}$ could provide strong constraints on the mass distribution, especially given the large sample size. The Large Synoptic Survey Telescope could provide these proper motions for the third and fourth Galactic quadrants, down to a limiting magnitude of $r = 24$, allowing stars to be surveyed all the way across the Galactic disk. Partial coverage of the first and second quadrants can be achieved with similar accuracies (though brighter limiting magnitude) by combining the Sloan Digital Sky Survey with the Palomar Observatory Sky Survey (Munn et al. 2004). This approach would offer an alternative, independent assessment of the mass distribution to complement the astrometric measurements described above.

5. Summary and Conclusions

In this paper, we examined how accurately we might be able to recover the mass distribution in the Galaxy (or more precisely, the gravitational force field in the Galactic disk) using current and near-future astrometric, photometric, and spectroscopic surveys of disk stars. We simulated observations of stars drawn from a simple model for the phase-space structure in an equilibrium, nonaxisymmetric disk and used a Markov Chain Monte Carlo approach to attempt to recover the model’s parameters. Our formulation of this method relied on finding the parameter set of the model that maximizes the probability of stars in a survey having their observed trigonometric parallax, proper motion, and line-of-sight velocity given their measured photometric parallax. Hence, it is immune to biases in sample selection. Indeed, with a correct representation of the error distributions for each observable and of the non-axisymmetric components of the mass distribution, no systematic errors were evident in our approach for samples of 100s-1000s of stars combining observed trigonometric parallaxes with errors in the range $1 \mu\text{as}$ to 2 mas (corresponding to proper motion errors assumed to be in the range $0.9 \mu\text{as yr}^{-1}$ to 1.2 mas yr^{-1}), photometric parallaxes known at

the 10%-20% level and line-of-sight velocity measurements accurate to 1 km s^{-1} .

The presence of non-axisymmetric features in the disk means that a precise mapping of the Galactic mass distribution will require a survey on global scales. Even in our simplified case with a single two-armed spiral pattern, restricting our survey to a limited range of Galactic longitude significantly reduced the accuracy of our results.

However, given such a global disk survey, we found that we could recover the mass profile in the range 4-20 kpc with a few percent accuracies using a variety of approaches. If μas trigonometric parallaxes are available (with associated proper-motion measurements and 1 km s^{-1} line-of-sight velocities), then this accuracy is feasible with a survey as small as a few hundred stars. Once trigonometric parallax errors exceed $10 \mu\text{as}$, the same accuracy can be achieved by supplementing the trigonometric parallaxes with photometric parallaxes accurate to 10%-20% and adopting a sample of thousands of stars, so long as proper-motion errors remain below a level of few hundred $\mu\text{as yr}^{-1}$. If proper-motion errors are of order a few mas yr^{-1} , then larger samples are needed in compensation.

We also found we could measure the mass distribution even in the absence of an accurate assessment of the distance to the Galactic center, R_0 . Including R_0 as a free parameter did increase our uncertainties by a factor of 2, but also allowed us to measure this distance with comparable accuracy to the mass distribution itself (i.e., a few percent for the samples discussed above).

We conclude that, whether one or all of the future surveys (e.g., SIM Lite, GAIA, VERA and APOGEE) are completed, a significant step forward in our understanding of the Galactic mass distribution (i.e., an assessment of the force field in the Galactic disk at the 1% level) is on the horizon, as well as detailed insights into disk dynamics.

These conclusions are based on the assumption that the deviations from a smooth axisymmetric model of the gravitational field in the disk can be modeled as a grand-design spiral pattern with a specified form (logarithmic spiral) and a well-defined pattern speed, without resonances within the disk. Further work is required to understand how relaxing these assumptions would affect the accuracy of astrometric disk surveys. Natural directions for future works are including vertical motions of sample stars as well as a bulge component, and more general models of spiral structure.

We acknowledge R. Patterson and J. Carlin for useful assistance with calculations regarding SIM and 2MASS. We thank L. S. Eyer for providing important insights into GAIA. We are grateful to M. Honma for the comments about VERA. We thank G. Zasowski for help with the dust extinction estimates used here. This work is supported by NASA/JPL contract

1228235 for the “Taking Measure of the Milky Way” key project of the Space Interferometry Mission.

REFERENCES

- Abadi, M. G., Navarro, J. F., Fardal, M., Babul, A., & Steinmetz, M. 2009, arXiv:0902.2477
- Allende Prieto, C., et al. 2008, *Astron. Nachr.*, 329, 1018
- Bailin, J., et al. 2005, *ApJ*, 627, L17
- Beers, T. C., Allende Prieto, C., Wilhelm, R., Yanny, B., & Newberg, H. 2004, *PASA*, 21, 207
- Binney, J., & Tremaine, S. 2008, *Galactic Dynamics* (2nd ed.; Princeton Univ. Press)
- Blitz, L. & Spergel, D. N. S. 1991, *ApJ*, 379, 631
- Chou, M., et al. 2007., *ApJ*, 670, 346
- Crézé, M., Chereul, E., Bienayme, O., & Pichon, C. 1998, *A&A*, 329, 920
- Debattista, V. P., Gerhard, O., & Sevenster, M. N. 2002, *MNRAS*, 334, 355
- de Blok, W. J. G. 2005, *ApJ*, 634, 227
- Dehnen, W., & Binney, J. J. 1998, *MNRAS*, 298, 387
- Dubinski, J. 1994 *ApJ*, 431, 617
- Eisenhauer, F., et al. 2003, *ApJ*, 597, L121
- Flynn, C., Holmberg, J., Portinari, L., Fuchs, B., & Jahreiß, H. 2006, *MNRAS*, 372, 1149
- Gilks, W. R., Richardson, S., & Spiegelhalter, D. J. 1996, *Markov Chain Monte Carlo in Practice* (London: Chapman and Hall)
- Gnedin, O. Y., Kravtsov, A. V., Klypin, A. A., & Nagai, D. 2004, *ApJ*, 616, 16
- Hachisuka, K., Brunthaler, A., Menten, K. M., Reid, M. J., Hagiwara, Y., & Mochizuki, N. 2009, *ApJ*, 696, 1981
- Hayashi, E., et al. 2004, *MNRAS*, 355, 794

- Hernquist, L. 1990, ApJS, 356, 359
- Hernquist, L. 1993, ApJS, 86, 389
- Holmberg, J., & Flynn, C. 2000, MNRAS, 313, 209
- Holmberg, J., & Flynn, C. 2004, MNRAS, 352, 440
- Honma, M., et al. 2000, PASJ, 52, 631
- Jurić, M., et al. 2008, ApJ, 673, 864
- Kazantzidis, S., Kravtsov, A. V., Zentner, A. R., Allgood, B., Nagai, D., & Moore, B. 2004, ApJ, 611, L73
- Kent, S.M. 1987, AJ, 93, 816
- Lewis, J. R., & Freeman, K. C. 1989, AJ, 97, 13
- Majewski, S. R., Skrutskie, M. F., Weinberg, M. D., & Ostheimer, J. C. 2003. ApJ, 599, 1082
- Munn, J. A., et al. 2004, AJ, 127, 3034
- Navarro, J. F., Frenk, C. S., & White, S. D. M. 1996, ApJ, 462, 563
- Navarro, J. F., Frenk, C. S., & White, S. D. M. 1997, ApJ, 490, 493
- Navarro, J. F., et al. 2004, MNRAS, 349, 1039
- Ojha, D. K., Bienaymé, O., Robin, A. C., & Mohan, V. 1994, A&A, 284, 810
- Olling, R. P., & Merrifield, M. R. 1998, MNRAS, 297, 943
- Perryman, M. A. C. 2002, Ap&SS, 280,1
- Quillen, A. C. 2002, AJ, 124, 924
- Reid, M. J. 2008, RevMexAA, 34, 53
- Reid, M. J., et al. 2009, arXiv:0902.3913v2
- Rygl, K. L. J., Brunthaler, A., Menten, K. M., Reid, M. J., & van Langevelde, H. J. 2008, arXiv:0812.0905v2
- Sellwood, J. A. 2006, ApJ, 637, 567

Steinmetz, M., et al. 2006, AJ, 132, 1645

Unwin, S. C., et al. 2007, 708, arXiv:0708.3953v2

Verde, L., et al. 2003, ApJS, 148,195

Weinberg, M. D. 1992, ApJ, 384, 81

Table 1. Parameters with INPUT values and an example OUTPUT.

Parameter	R_i (kpc)	INPUT	OUTPUT	1σ Error
$M_1(10^{10}M_\odot)$	4.00	2.37	2.24	0.15
$M_2(10^{10}M_\odot)$	6.29	4.94	4.90	0.10
$M_3(10^{10}M_\odot)$	8.57	7.86	7.77	0.12
$M_4(10^{10}M_\odot)$	10.86	10.92	10.76	0.16
$M_5(10^{10}M_\odot)$	13.14	13.99	13.83	0.17
$M_6(10^{10}M_\odot)$	15.43	16.99	17.10	0.27
$M_7(10^{10}M_\odot)$	17.71	19.90	19.72	0.30
$M_8(10^{10}M_\odot)$	20.00	22.68	22.77	0.33
$\sigma_{R,\odot}(\text{km s}^{-1})$	—	25.00	24.64	0.64
ϕ_0 (rad)	—	1.83	1.85	0.07
c (rad)	—	7.46	7.51	0.17
Ω_p ($\text{km s}^{-1} \text{kpc}^{-1}$)	—	1.40	1.12	0.37
$\Phi_a(\text{km s}^{-1})^2$	—	200.0	208.3	32.8
h_σ (kpc)	—	3.00	3.14	0.10
h (kpc)	—	3.00	3.36	0.35
R_0 (kpc)	—	8.00	7.97	0.12

Note. — Recovered OUTPUT parameters and 1σ errors for a survey with $\delta_{p,\text{phot}} = 0.15p$ and $\delta_{p,\text{tri}} = 10 \mu\text{as}$ and $N = 850$ stars. M_i is the mass within R_i .

Table 2. Mean errors of parameters Versus number of stars N .

N	\bar{M}	$\sigma_{R,\odot}$	ϕ_0	c	Ω_p	Φ_a	h_σ	h	R_0
500	0.17	0.79	0.08	0.23	0.54	48.2	0.12	0.44	—
850	0.13	0.60	0.06	0.17	0.41	36.7	0.09	0.29	—
2000	0.08	0.39	0.04	0.10	0.30	27.5	0.06	0.19	—
4000	0.06	0.28	0.02	0.07	0.20	19.1	0.04	0.12	—
8000	0.04	0.20	0.02	0.05	0.13	12.4	0.03	0.09	—
500	0.27	0.88	0.09	0.22	0.52	44.8	0.12	0.43	0.16
850	0.21	0.66	0.07	0.17	0.42	37.5	0.09	0.32	0.12
2000	0.13	0.42	0.05	0.11	0.30	27.2	0.06	0.19	0.08
4000	0.09	0.30	0.03	0.07	0.21	19.1	0.04	0.13	0.05
8000	0.07	0.21	0.02	0.05	0.13	11.7	0.03	0.09	0.04

Note. — The means of the estimated error of parameters are calculated from 10 runs of MCMC for the case of $\delta_{p,\text{tri}} = 10 \mu\text{as}$, either fixing $R_0 = 8$ kpc (shown as —) or fitting R_0 . Units are same as in Table 1. For \bar{M} , the mean is also taken over $i = 1-8$. See the notes for Table 1.

Table 3. Mean errors of parameters with various trigonometric parallax errors $\delta_{p,\text{tri}}$.

$\delta_{p,\text{tri}}$	\bar{M}	$\sigma_{R,\odot}$	ϕ_0	c	Ω_p	Φ_a	h_σ	h
1	0.10	0.58	0.05	0.13	0.33	32.8	0.07	0.22
2	0.10	0.57	0.05	0.14	0.34	33.5	0.08	0.26
4	0.11	0.58	0.05	0.14	0.40	37.3	0.08	0.28
8	0.12	0.59	0.06	0.16	0.41	37.3	0.09	0.29
10	0.13	0.60	0.06	0.17	0.41	36.7	0.09	0.29
20	0.14	0.61	0.06	0.18	0.43	38.2	0.09	0.32
50	0.15	0.63	0.06	0.18	0.44	38.2	0.10	0.35
100	0.15	0.65	0.06	0.18	0.45	39.0	0.10	0.37
200	0.16	0.65	0.06	0.19	0.45	38.7	0.11	0.38
500	0.18	0.67	0.06	0.20	0.47	40.3	0.12	0.40
1000	0.23	0.68	0.07	0.22	0.50	41.8	0.14	0.54
2000	0.31	0.74	0.07	0.23	0.56	46.1	0.15	0.57

Note. — For $N = 850$ and fixing $R_0 = 8$ kpc. See the notes for Table 2.

Table 4. Mean errors of parameters with various photometric parallax errors $\delta_{p,\text{phot}}$.

$\delta_{p,\text{tri}}$	$\delta_{p,\text{phot}}$	\bar{M}	$\sigma_{R,\odot}$	ϕ_0	c	Ω_p	Φ_a	h_σ	h
10	0.10	0.14	0.60	0.06	0.17	0.48	42.0	0.09	0.45
10	0.15	0.13	0.60	0.06	0.17	0.41	36.7	0.09	0.29
10	0.20	0.12	0.59	0.05	0.15	0.39	37.6	0.09	0.23
1000	0.10	0.23	0.66	0.06	0.21	0.51	40.5	0.12	1.07
1000	0.15	0.23	0.68	0.07	0.22	0.50	41.8	0.14	0.54
1000	0.20	0.23	0.70	0.06	0.20	0.47	41.0	0.14	0.37

Note. — For $N = 850$ and fixing $R_0 = 8$ kpc. $\delta_{p,\text{tri}}$ is in μas . See the notes for Table 2.

Table 5. Mean errors of parameters with various angular coverages ϕ_{max} .

N	ϕ_{max}	\bar{M}	$\sigma_{R,\odot}$	c	ϕ_0	Ω_p	Φ_a	h_σ	h	R_0
850	133	0.13	0.60	0.06	0.17	0.41	36.7	0.09	0.29	—
850	90	0.13	0.61	0.06	0.17	0.41	37.6	0.09	0.29	—
850	60	0.14	0.58	0.05	0.17	0.39	37.4	0.09	0.36	—
850	30	0.18	0.59	0.06	0.20	0.37	35.6	0.08	0.48	—
850	20	0.22	0.58	0.07	0.22	0.42	39.8	0.08	0.46	—
850	10	0.40	0.58	0.06	0.20	0.45	43.4	0.08	0.57	—
850	133	0.21	0.66	0.07	0.17	0.42	37.5	0.09	0.32	0.12
850	90	0.25	0.68	0.08	0.17	0.41	37.7	0.09	0.33	0.16
850	60	0.37	0.72	0.11	0.19	0.41	39.6	0.09	0.38	0.24
850	30	0.79	1.15	0.24	0.34	0.44	41.4	0.08	0.40	0.56
2000	133	0.08	0.39	0.04	0.10	0.30	27.5	0.06	0.19	—
2000	90	0.08	0.39	0.04	0.11	0.28	26.7	0.06	0.21	—
2000	60	0.09	0.39	0.04	0.12	0.28	26.5	0.06	0.23	—
2000	30	0.12	0.39	0.04	0.13	0.30	29.5	0.06	0.25	—
2000	20	0.15	0.37	0.04	0.13	0.29	29.1	0.05	0.27	—
2000	10	0.25	0.38	0.04	0.14	0.31	29.6	0.05	0.29	—
2000	133	0.13	0.42	0.05	0.11	0.30	27.2	0.06	0.19	0.08
2000	90	0.16	0.42	0.05	0.11	0.26	24.5	0.06	0.23	0.10
2000	60	0.23	0.59	0.07	0.13	0.28	28.0	0.06	0.26	0.16
2000	30	0.66	0.61	0.22	0.31	0.34	30.6	0.05	0.27	0.49
2000	20	0.92	0.61	0.29	0.38	0.36	33.6	0.05	0.31	0.67

Note. — The case of $\delta_{p,\text{tri}} = 10 \mu\text{as}$. MCMC fails to converge for $\phi_{\text{max}} \leq 20^\circ$ and $\leq 10^\circ$ for $N = 850$ and 2000, respectively, in the case where R_0 is fitted. “—” means that R_0 is fixed. See the notes for Table 2.

Table 6. Number of observable stars by SIM Lite in 240 hr with various extinctions and limiting magnitude.

$\delta_{p,\text{tri}}$ (μas)	$\frac{A_{V,\text{win}}}{A_{V,\text{typ}}}$	$N(V_1[\text{mag}])$						
		$V_1=20$	$V_1=19$	$V_1=18$	$V_1=17$	$V_1=16$	$V_1=15$	$V_1=14$
8	1.0	24	—	—	—	—	—	—
8	0.8	37	70	—	—	—	—	—
8	0.5	72	129	213	336	—	—	—
8	0.3	127	213	323	458	631	833	—
8	0.0	177	360	566	777	957	1069	1131
10	1.0	45	—	—	—	—	—	—
10	0.8	69	128	—	—	—	—	—
10	0.5	132	225	354	521	—	—	—
10	0.3	224	355	505	669	853	1031	—
10	0.0	304	550	779	969	1108	1182	1215
20	1.0	119	—	—	—	—	—	—
20	0.8	172	296	—	—	—	—	—
20	0.5	305	470	656	864	—	—	—
20	0.3	474	664	835	996	1126	1212	—
20	0.0	584	856	1030	1147	1211	1235	1237
100	1.0	295	—	—	—	—	—	—
100	0.8	399	594	—	—	—	—	—
100	0.5	613	807	974	1108	—	—	—
100	0.3	808	969	1083	1163	1209	1233	—
100	0.0	900	1079	1166	1212	1231	1237	1237

Note. — The numbers of observable stars $N(V_1[\text{mag}])$ are estimated by using the required mission time for SIM Lite given by Figure 9. A factor $A_{V,\text{win}}/A_{V,\text{typ}}$ indicates the fraction of V -band extinction at low extinction window relative to the typical extinction in that direction (see Section 4.1.1). V_1 represents V -band limiting magnitude to select sample stars. “—” means that stars can not be sampled in all R_i bins with that V_1 .

Table 7. $\bar{\delta}_M$ by SIM Lite in 240 hr with various extinctions and limiting magnitude.

$\delta_{p,\text{tri}}$ (μas)	$\frac{A_{V,\text{win}}}{A_{V,\text{typ}}}$	$\bar{\delta}_M$			
		$V_1=20$	$V_1=19$	$V_1=18$	$V_1=17$
100	1.0	0.311	—	—	—
100	0.8	0.238	0.216	—	—
100	0.5	0.178	0.161	0.149	0.156

Note. — $\bar{\delta}_M$ are estimated for the cases given in Table 6 with $\delta_{p,\text{tri}} = 100 \mu\text{as}$ and fixing R_0 . The survey regions are as shown in Figure 10. The numbers of sample stars are as in Table 6.

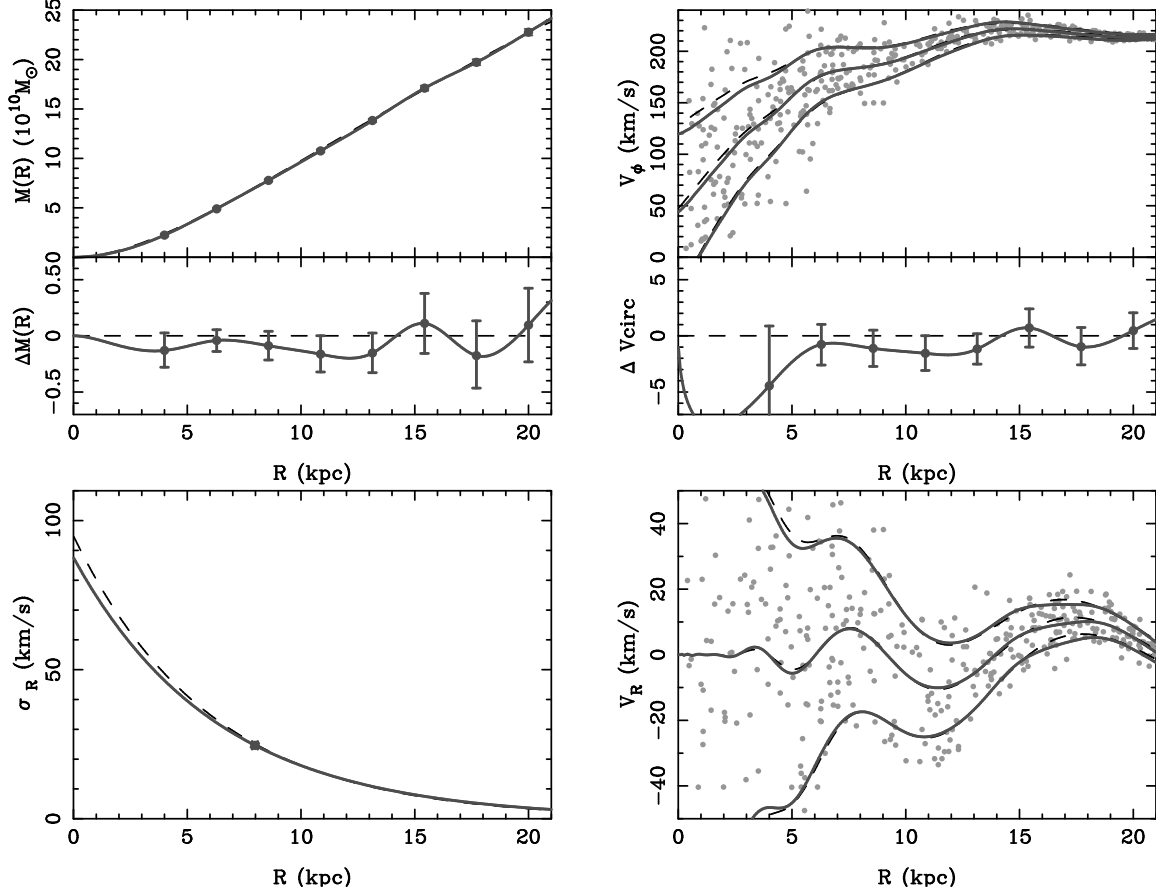


Fig. 1.— INPUT (dashed lines) and recovered OUTPUT (solid lines with $\pm 1\sigma$ dispersion) models as a function of the Galactocentric radius R . The OUTPUT is derived for samples of $N = 850$ stars, observed with assumed photometric parallax and trigonometric parallax accuracies of $\delta_{p,\text{phot}} = 0.15p$ and $\delta_{p,\text{tri}} = 10 \mu\text{as}$. The model curves are interpolated from the mass parameters, M_i (indicated for the OUTPUT as points with 1σ error bars). The oscillations in v_R are due to spiral arms. Top-left: mass within R , $M(R)$. Middle left: residual from the INPUT mass, $\Delta M(R)$. Top right: azimuthal velocity v_ϕ . Middle right: residual from the INPUT circular velocity, Δv_{circ} . Bottom left: radial velocity dispersion σ_R , which is estimated from Equation (9) using OUTPUT $\sigma_{R,\odot}$ and h_σ . Bottom right: radial velocity v_R . The values of v_ϕ and v_R for stars with $\phi = \pm\pi/16$ are plotted as light gray dots. In some plots the error bars are too small to be resolved and the dashed and solid lines lie on top of one another. We can recover the mass to within $\sim 2\%$ for $R=4\text{-}20$ kpc.

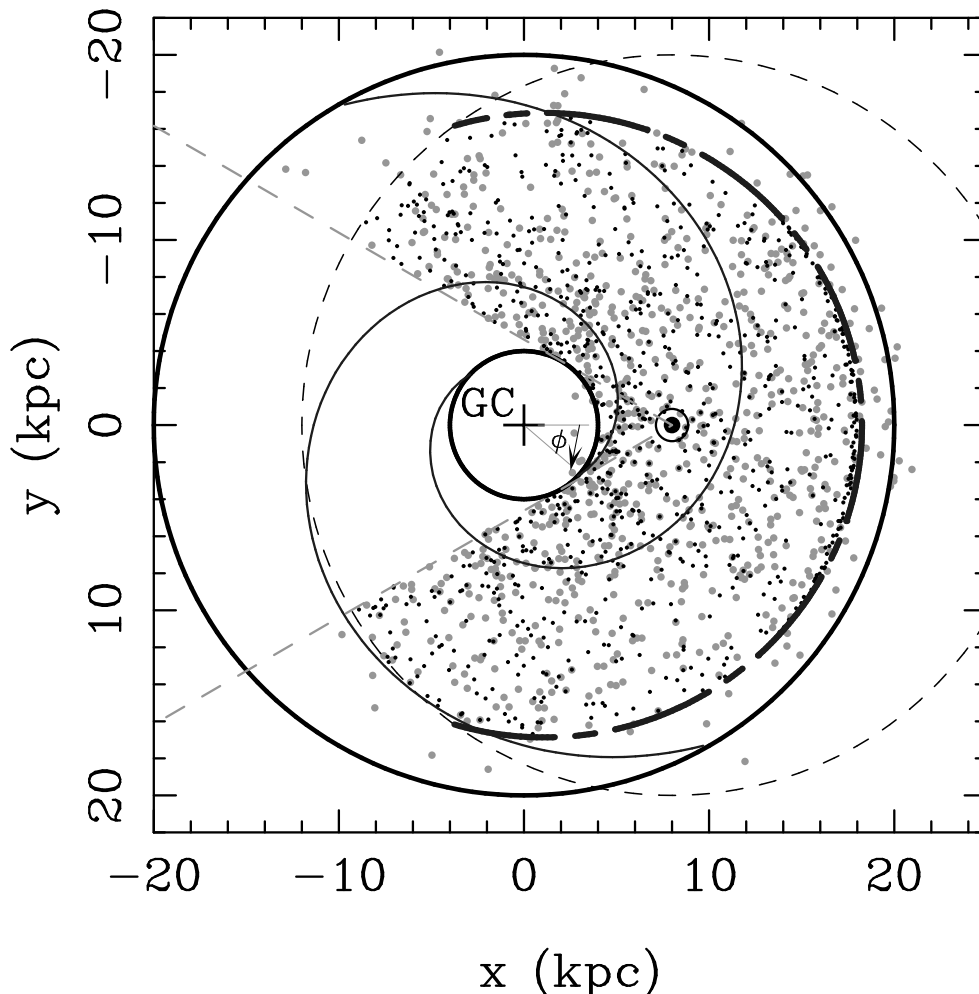


Fig. 2.— Spatial distribution of selected stars on the Galactic plane seen from the North Galactic Pole. The large gray dots indicate their intrinsic positions and the small black dots represent their positions derived from their “observed” photometric parallax. The sample is chosen from their observed positions so that there are equal numbers of stars in the seven bins defined by the Galactocentric radii R_i (Section 2.1.3). The symbols + and \odot indicate the GC and the Sun. We use stars (small black dots) between 4 (inner thick circle) and 18 kpc from the GC and < 20 kpc from the Sun (dashed circle). We also select only stars within $20 \text{ kpc} - 0.17d$ from the GC (short-long dashed line) to reduce the number of stars that leak outside the outermost model radius $R_8 = 20$ kpc due to errors in the photometric parallax (see details in Section 2.1.3). Stars that lie behind the GC with $|l| < 30^\circ$ (dashed lines) are not used. The peak of the spiral arm potential is also drawn. The angle ϕ is defined as shown by the arrow.

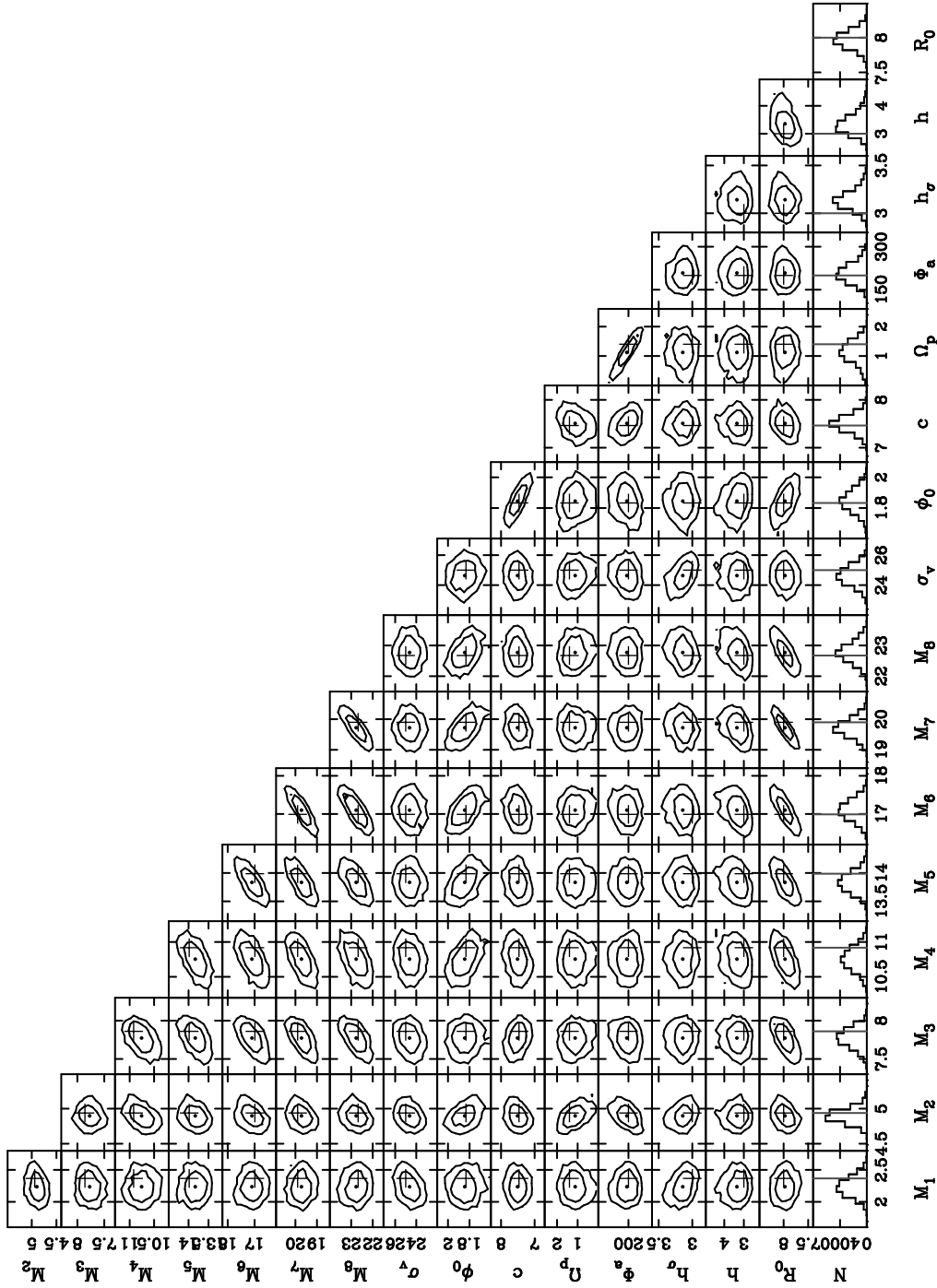


Fig. 3.— Likelihood distribution of parameters for the MCMC run shown in Figure 1, with $N = 850$, $\delta_{p,\text{phot}} = 0.15p$ and $\delta_{p,\text{tri}} = 10 \mu\text{as}$. The dots indicate the maximum likelihood values. The crosses indicate the INPUT values. The contours indicate 68% and 95% confidence intervals. The histograms represent the projected likelihood distribution for each parameter, where the vertical lines indicate INPUT values.

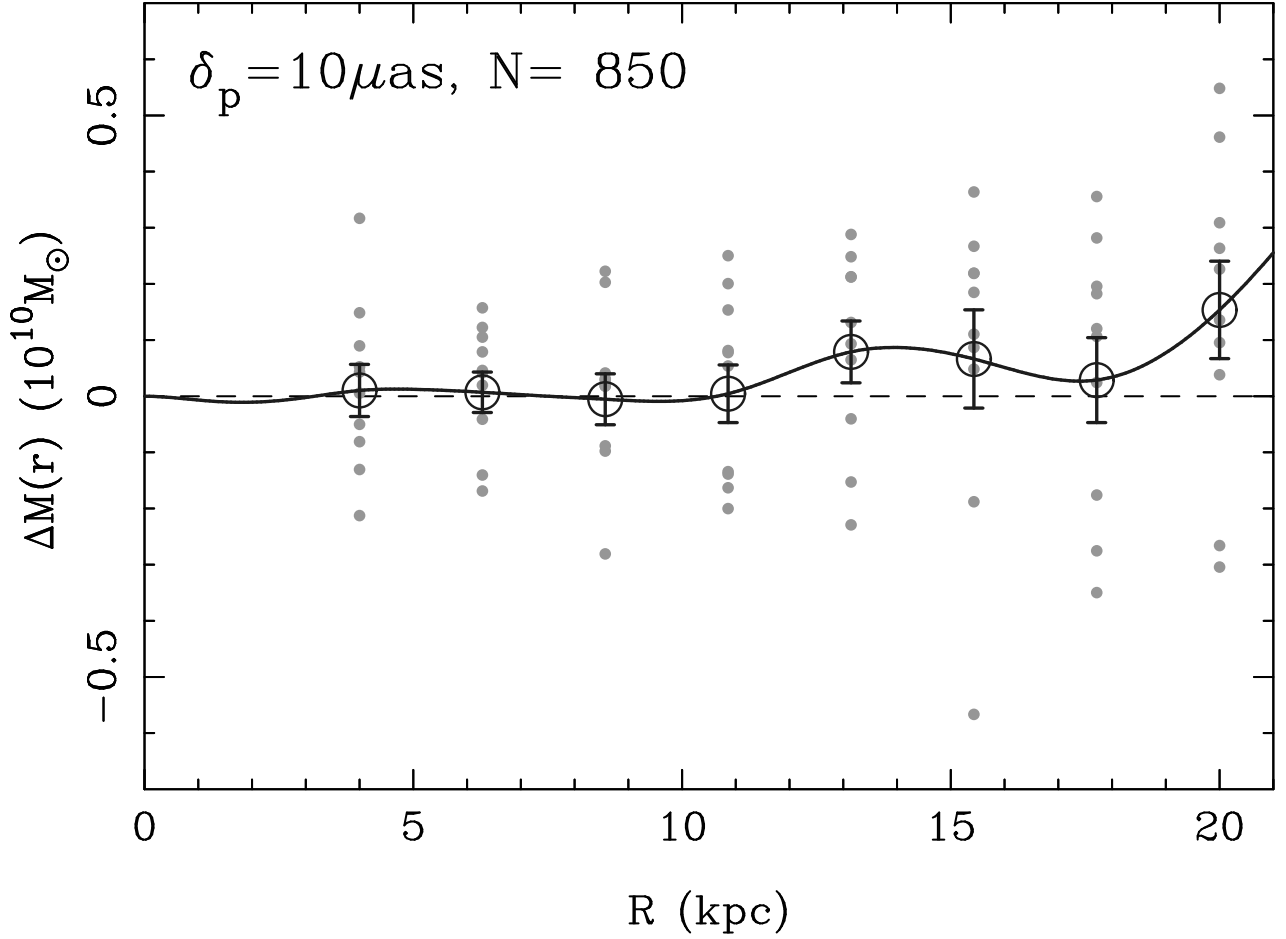


Fig. 4.— Residuals from INPUT mass, ΔM_i , of 10 MCMC runs as a function of R (gray dots), as in the middle left panel of Figure 1, $N = 850$, $\delta_{p,\text{phot}} = 0.15p$ and $\delta_{p,\text{tri}} = 10 \mu\text{as}$. The distance to the GC, R_0 , is one of the fitting parameters. Here, each run uses an independent sample of simulated stars. The open circles with error bars indicate the mean of 10 runs with 1σ errors. The solid line is the interpolation of the mean ΔM_i . One can see that any systematic differences are within the error, $\sim 0.1 \times 10^{10} M_\odot$.

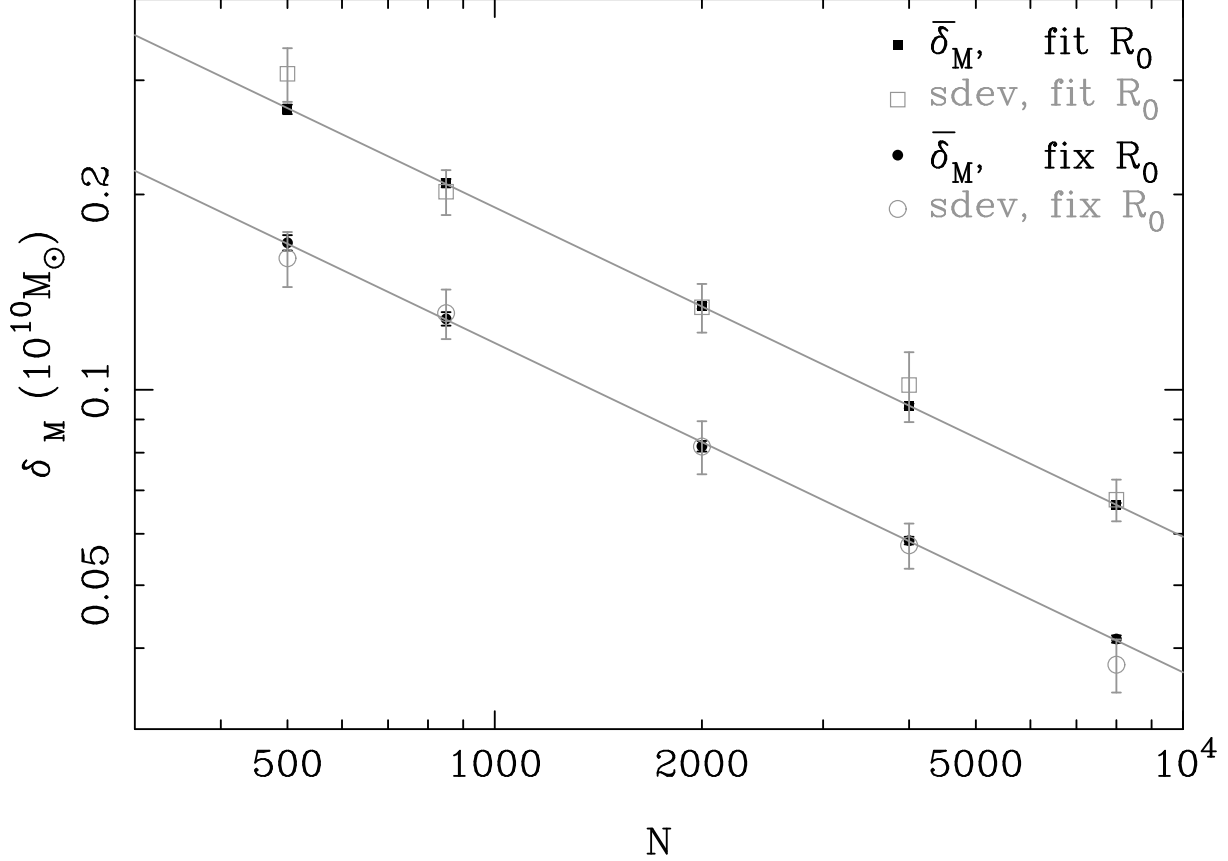


Fig. 5.— Mean of errors in M_i calculated by the MCMC ($\bar{\delta}_M$: filled symbols) and the standard deviation of estimates from an ensemble of 10 runs (sdev: open symbols with error bars) as a function of the number of stars, N , for $\delta_{p,\text{phot}} = 0.15p$, $\delta_{p,\text{tri}} = 10 \mu\text{as}$. The squares denote runs in which R_0 was fitted and the circles denote runs in which R_0 was fixed at 8 kpc. Here the mean of δ_M and *sdev* is taken over $i = 1-8$ and over 10 runs of MCMC. The solid lines indicate the scaling $\delta M / (10^9 M_\odot \times \sqrt{500/N}) = 1.7$ and 2.7 , respectively.

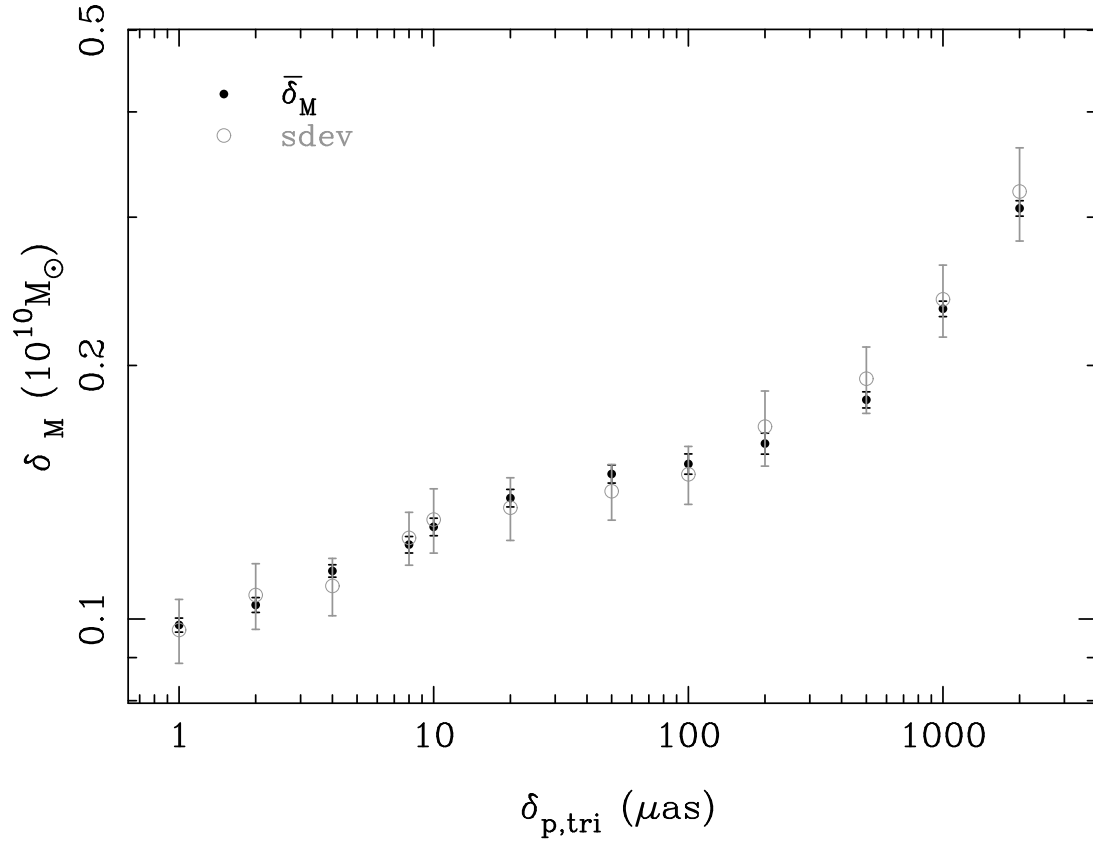


Fig. 6.— Mean of estimated errors in M_i and the standard deviation from the true M_i as a function of trigonometric parallax error for sample size $N = 850$, $\delta_{p,\text{phot}} = 0.15p$ and $\delta_{p,\text{tri}} = 10 \mu\text{as}$. In these runs R_0 is fixed at 8 kpc.

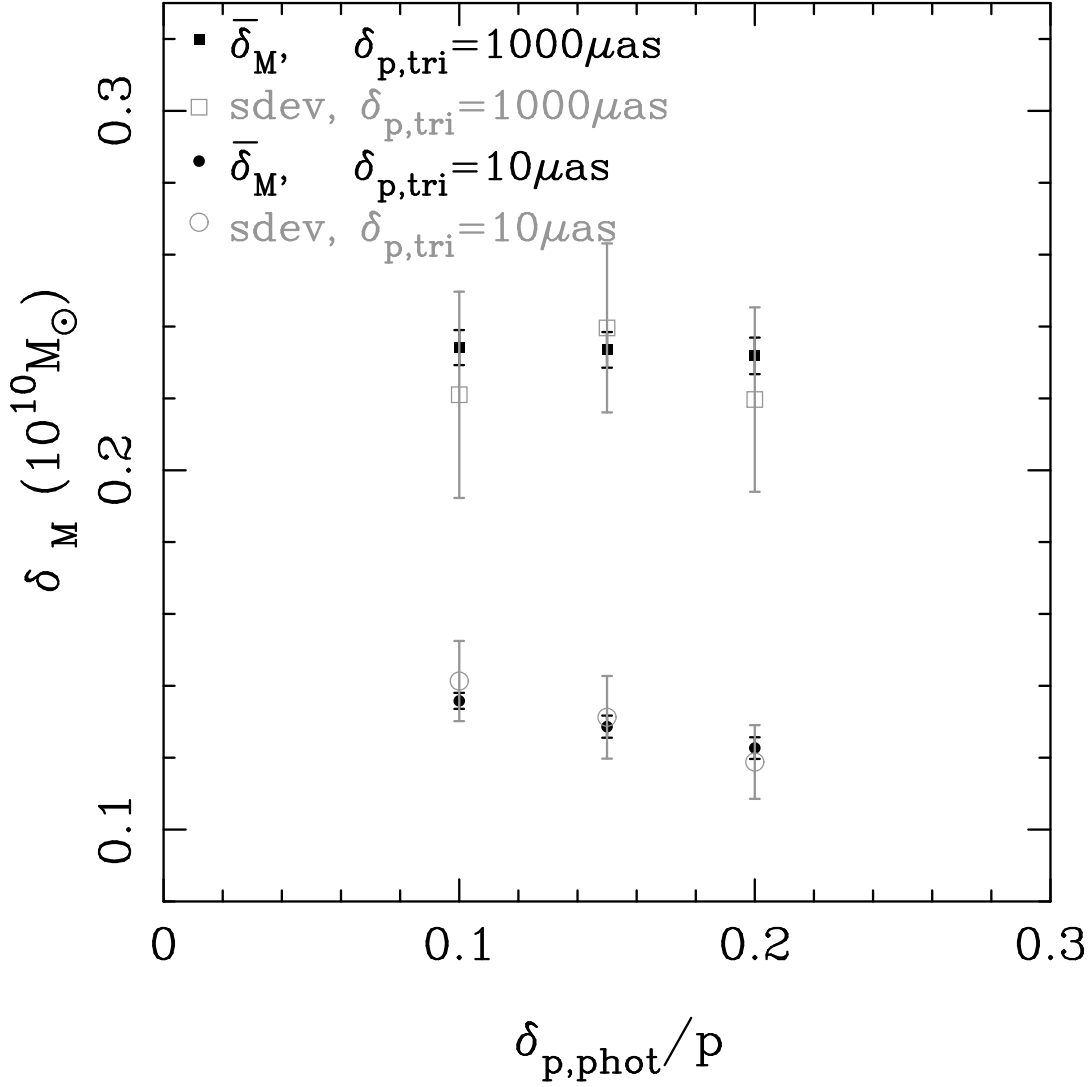


Fig. 7.— Mean of estimated errors in M_i (filled symbols) and the standard deviation from the true M_i (open symbols) as a function of relative photometric parallax error $\delta_{p,\text{phot}}/p$ for $N = 850$, $\delta_{p,\text{tri}} = 10 \mu\text{as}$ (circle) and $\delta_{p,\text{tri}} = 1000 \mu\text{as}$ (square). In these runs R_0 is fixed at 8 kpc. Note that in some cases the error in derived quantity goes down as the observational error goes up (see discussion in Section 3.4).

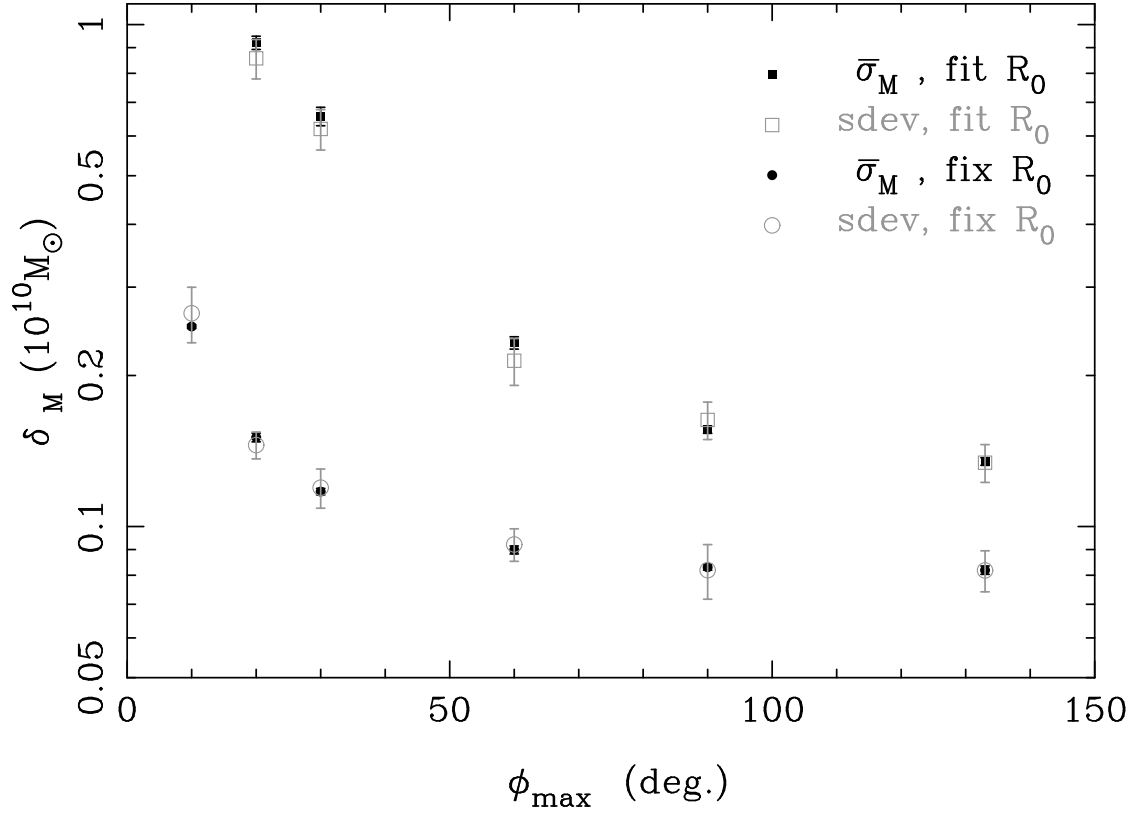


Fig. 8.— Mean estimated error in M_i (filled symbols) and the standard deviation from the true M_i (open symbols) for $N = 2000$ as a function of ϕ_{\max} . The circles and squares are for the case of fixing $R_0 = 8$ kpc and fitting R_0 , respectively. The MCMC fails to converge for $\phi_{\max} \leq 10^\circ$ when R_0 is fitted. Covering $\phi_{\max} \geq 60^\circ$ is required to recover models efficiently, especially for the case of fitting R_0 .

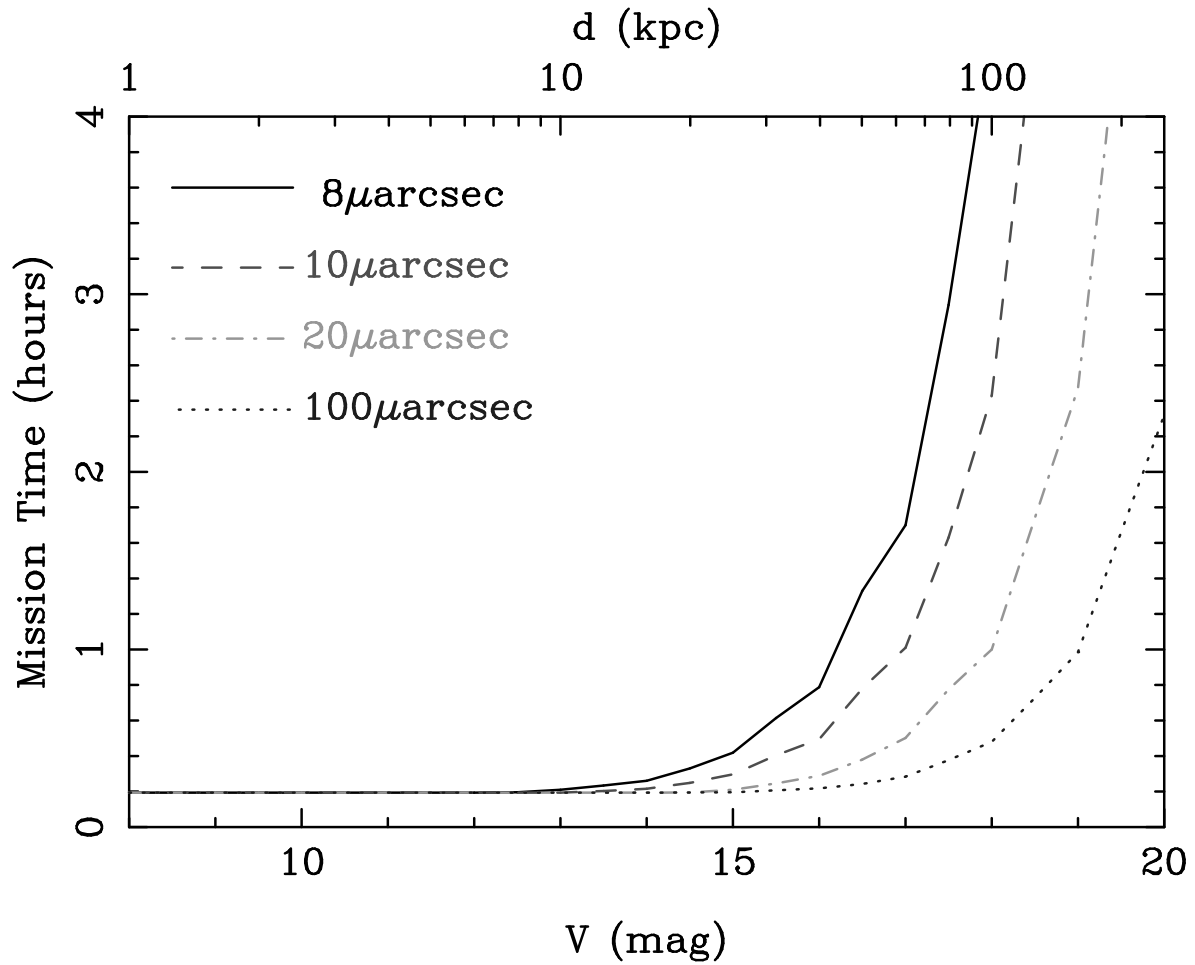


Fig. 9.— SIM Lite’s required mission time to measure the parallax of a star with 8, 10, 20 and 100 μas accuracy as a function of V-band magnitude of the star. The top horizontal axis indicates the distance to the target with an absolute magnitude of $M_V = -2$ mag (e.g., M giants).

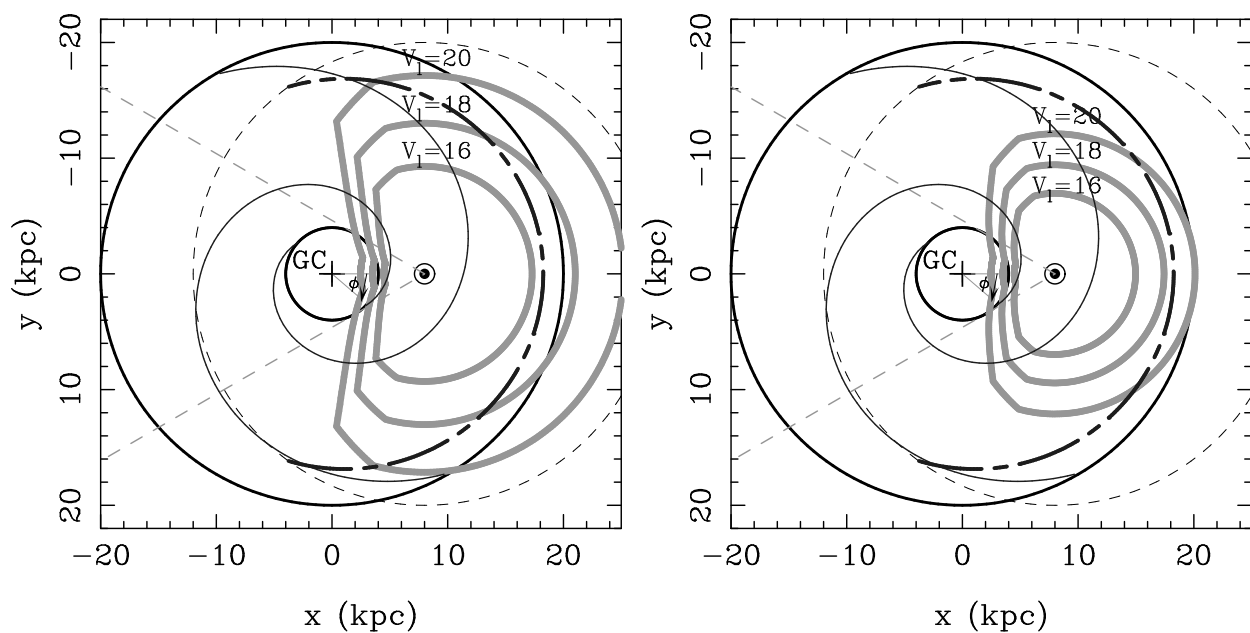


Fig. 10.— Same as Figure 2, but showing the maximum survey region with the V -band limiting magnitude $V_l = 16, 18$ and 20 mag (the thick gray lines) for the case that we observe M-giants with an absolute magnitude of $M_V = -2$ through the low extinction windows with $A_{V,\text{win}}/A_{V,\text{typ}} = 0.5$ (left panel) and 0.8 (right panel) (see details in Section 4.1.1).